Article

Developmental Cell

Disrupted endosomal trafficking of the Vangl-Celsr polarity complex underlies congenital anomalies in *Xenopus* trachea-esophageal morphogenesis

Graphical abstract

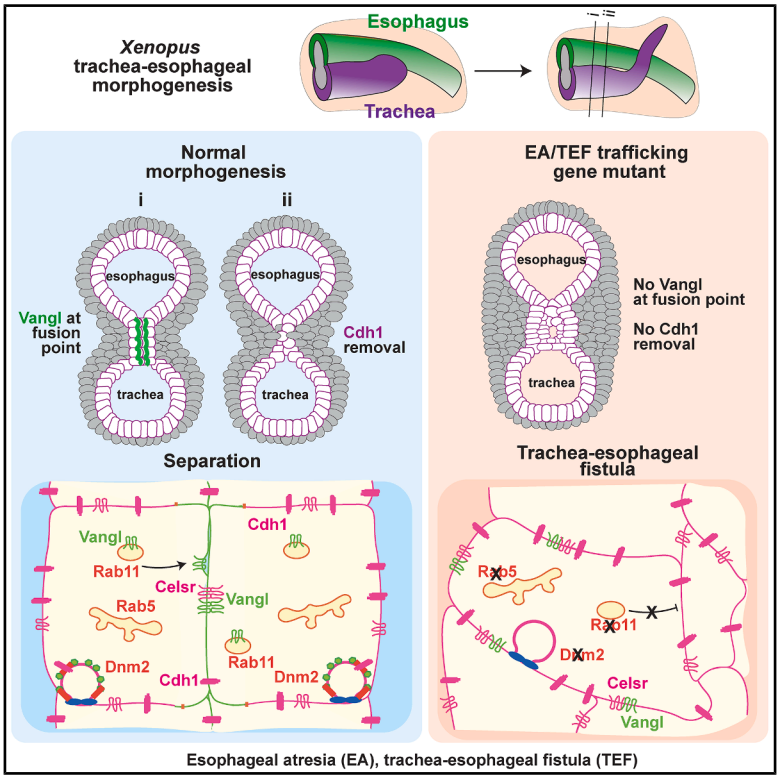

Highlights

- Esophgeal atresia patients have *de novo* variants enriched in intracellular trafficking genes
- Mutating patient genes in *Xenopus* disrupts tracheoesophageal separation
- Asymmetric endocytosis of Cdh1 is required for foregut separation
- Rab11a endosomes transport Vangl2 to maintain apical memory in fused epithelia

Authors

Nicole A. Edwards, Scott A. Rankin, Adhish Kashyap, ..., Yufeng Shen, Wendy K. Chung, Aaron M. Zorn

Correspondence

nicole.edwards@cchmc.org (N.A.E.), aaron.zorn@cchmc.org (A.M.Z.)

In brief

Edwards et al. identify an endosome-cell polarity pathway required for trachea-esophageal morphogenesis in *Xenopus* and show that failure of Rab11a-endosome-mediated trafficking of Vangl2 to the contact point of fused epithelial cells results in trachea-esophageal fistulas. These findings have implications for fusion-fission events in organogenesis and congenital anomalies.

Edwards et al., 2025, Developmental Cell *60*, 2487–2502
September 22, 2025
https://doi.org/10.1016/j.devcel.2025.04.026

CellPress

Developmental Cell

CellPress
OPEN ACCESS

Article

Disrupted endosomal trafficking of the Vangl-Celsr polarity complex underlies congenital anomalies in *Xenopus* trachea-esophageal morphogenesis

Nicole A. Edwards,[1,*] Scott A. Rankin,[1] Adhish Kashyap,[1] Alissa Warren,[1] Zachary N. Agricola,[1,2] Alan P. Kenny,[2] Matthew Kofron,[1,3] Yufeng Shen,[4,5] Wendy K. Chung,[6,7] and Aaron M. Zorn[1,3,8,*]

[1]Center for Stem Cell and Organoid Medicine (CuSTOM), Perinatal Institute, Division of Developmental Biology, Cincinnati Children's Hospital Medical Center, Cincinnati, OH 45229, USA
[2]Perinatal Institute, Division of Neonatology, Cincinnati Children's Hospital Medical Center, Cincinnati, OH 45229, USA
[3]Department of Pediatrics, University of Cincinnati College of Medicine, Cincinnati, OH 45267, USA
[4]Department of Systems Biology, Columbia University Irving Medical Center, New York, NY 10032, USA
[5]Department of Biomedical Informatics, Columbia University Irving Medical Center, New York, NY 10032, USA
[6]Department of Pediatrics, Boston Children's Hospital, Harvard Medical School, Boston, MA 02115, USA
[7]Departments of Pediatrics and Medicine, Columbia University Irving Medical Center, New York, NY 10032, USA
[8]Lead contact
*Correspondence: nicole.edwards@cchmc.org (N.A.E.), aaron.zorn@cchmc.org (A.M.Z.)
https://doi.org/10.1016/j.devcel.2025.04.026

SUMMARY

Disruptions in foregut morphogenesis can result in life-threatening conditions where the trachea and esophagus fail to separate, such as esophageal atresia (EA) and tracheoesophageal fistulas (TEFs). The developmental basis of these congenital anomalies is poorly understood, but recent genome sequencing reveals that *de novo* variants in intracellular trafficking genes are enriched in EA/TEF patients. Here, we confirm that mutation of orthologous genes in *Xenopus* disrupts trachea-esophageal separation similar to EA/TEF patients. The Rab11a recycling endosome pathway is required to localize Vangl-Celsr polarity complexes at the luminal cell surface where opposite sides of the foregut tube fuse. Partial loss of endosomal trafficking or Vangl-Celsr complexes disrupts epithelial polarity and cell division orientation. Mutant cells accumulate at the fusion point, fail to relocalize cadherin, and do not separate into distinct trachea and esophagus. These data provide insights into the mechanisms of congenital anomalies and general paradigms of tissue fusion during organogenesis.

INTRODUCTION

Esophageal atresia (EA) and tracheoesophageal fistulas (TEFs), which affect approximately 1 in 3,000 newborns, are life-threatening congenital anomalies that arise when the embryonic foregut does not separate correctly into distinct trachea and esophageal tubes.[1–3] This results in esophageal discontinuity (EA) and/or a pathological connection between the trachea and esophagus (TEF). Rarer are laryngeal-tracheal-esophageal clefts, where, in some extreme cases, the foregut fails to separate along its entire length, essentially resulting in a complete TEF.[4] Roughly half of EA/TEF patients also have variably penetrant co-occurring anomalies in other organs, including gastrointestinal, pulmonary, cardiovascular, renal, and central nervous system, suggesting undefined syndromes.[5,6] The genetic etiology of tracheoesophageal anomalies is poorly understood and is associated with spontaneous *de novo* variants, chromosomal rearrangements, copy number variation, indels, and single nucleotide changes in affected newborns.[1,7] Known variants only account for 10%–15% of cases worldwide, with the remaining having no identified risk gene. Even when the causative variants are known, why they result in tracheoesophageal anomalies is unclear because the cellular mechanisms governing foregut morphogenesis are poorly understood.

Tracheoesophageal morphogenesis begins when the foregut endoderm is patterned along the dorsal-ventral axis by an evolutionarily conserved Hedgehog-Wnt-Bmp signaling network, resulting in dorsal Sox2+ esophageal progenitors and ventral Nkx2-1+ respiratory progenitors.[8–11] After patterning, the foregut constricts at the midline, and a population of epithelial cells on either side of the foregut tube that express both dorsal and ventral markers (Sox2/Nkx2-1/Islet1) come together and adhere, forming a transient epithelial bilayer.[12,13] Epithelial cells at the fusion point then progressively lose adhesion to one another and integrate into either the ventral or dorsal foregut as the surrounding Foxf1+ splanchnic mesoderm invades between the nascent trachea and esophagus.[13] Thus, the single foregut epithelial tube fuses, reorganizes its cellular junctions, and then

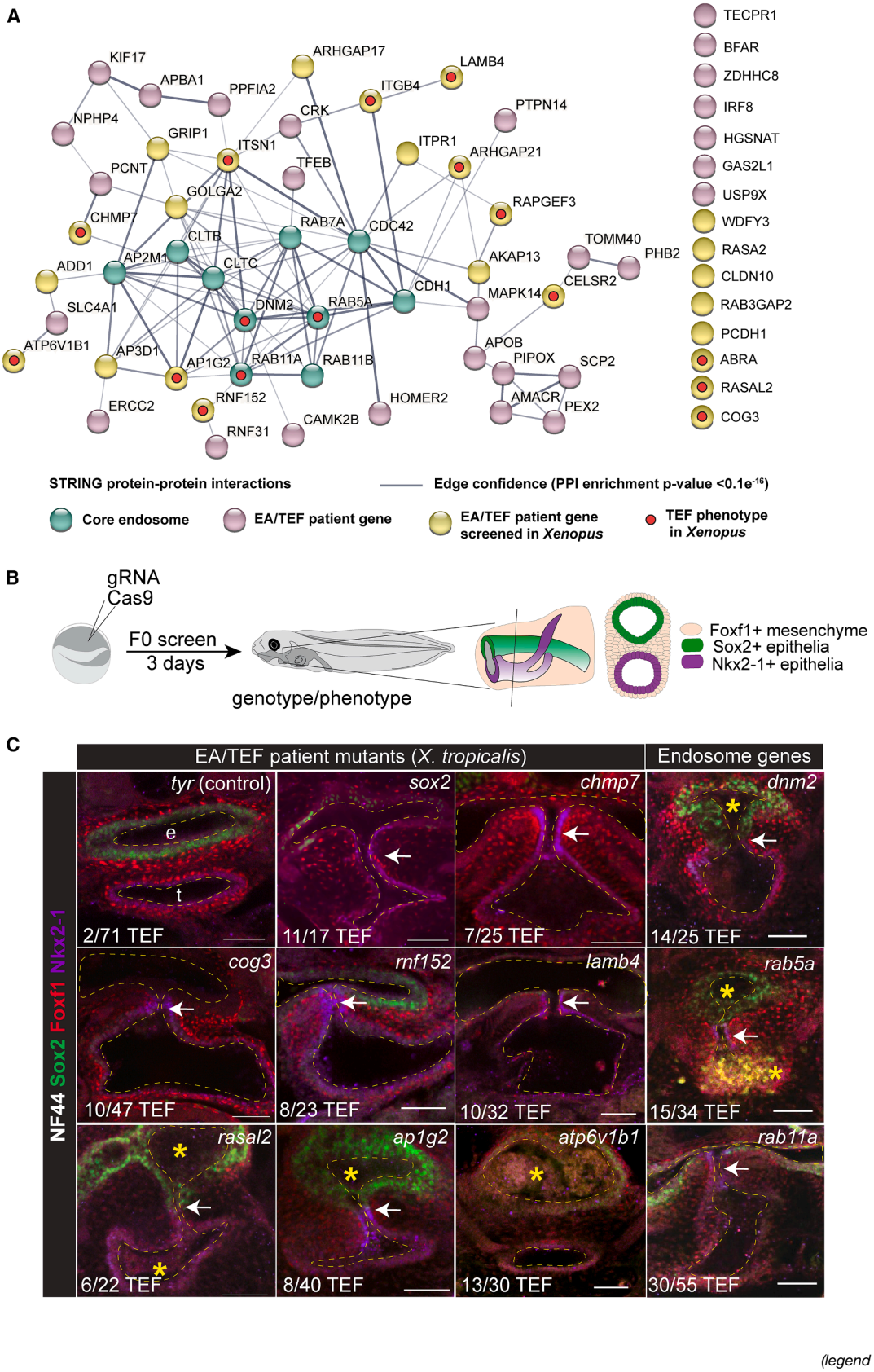

(legend on next page)

undergoes fission with coordinated cell rearrangements to reconnect the epithelia into two separate tubes. How cell signaling and transcription factors regulate the cellular processes of tracheoesophageal morphogenesis is unclear.

Similar epithelial fusion and fission events are crucial for the morphogenesis of many tissues, including the heart, oral palate, eyes, inner ear, urogenital sinus, and neural tube, organ systems that can also be disrupted in complex EA/TEF patients, suggesting shared biological mechanisms.[14] Such tissue fusion and fission events involve dynamic and coordinated changes in cell adhesion and polarity.[14,15] For instance, studies of vertebrate neural tube closure and *Drosophila* retina morphogenesis indicate that the precise spatial and temporal coordination of cell adhesion and cell polarity across different epithelial populations is essential for proper tissue fusion. A remaining challenge in the field is understanding how the proteins involved in cell adhesion, cell polarity, and cell junctions are orchestrated to regulate epithelial remodeling during morphogenesis.[16–19] We recently found in *Xenopus* that Rab11+ recycling endosomes somehow regulate tracheoesophageal morphogenesis downstream of Hedgehog signaling.[13] Rab11 is a small GTPase required for the intracellular recycling of endosomal vesicles that cells use to transport newly synthesized proteins from the Golgi to the plasma membrane and to change the composition of specific plasma membrane domains by internalizing receptors and other cell surface proteins.[20] How recycling endosomes regulate epithelial remodeling in the foregut was unknown. However, recent whole-genome sequencing of EA/TEF patients who exhibit complex multi-organ phenotypes revealed an enrichment of potentially damaging *de novo* variants in genes involved in endocytosis and intracellular trafficking.[21] This finding and our previous observations prompted us to test the hypothesis that endosomal trafficking represents a critical morphogenetic bottleneck in tracheoesophageal separation and to explore the underlying cellular mechanisms.

Here, we demonstrate that the Rab11a recycling endosome pathway is required upstream of the Vangl-Celsr cell polarity complex for proper fission of the fused foregut tube. Mechanistically, Rab11a localizes the transmembrane protein Vangl2 to the midline luminal cell surface where juxtaposing apical sides of the foregut touch, localize cadherin, and adhere to one another to form the transient epithelial bilayer. Rab11a and Vangl-Celsr complexes enriched at the contact surface appear to confer an ‘‘apical memory’’ essential for maintaining the transient bilayer and its subsequent resolution. A partial loss of (1) core endosomal trafficking components, (2) orthologs of EA/TEF patient risk genes, or (3) the Vangl-Celsr proteins disrupt cell polarity and the orientation of cell division in the transient bilayer. Mutant cells accumulate in a disorganized septum, fail to internalize E-cadherin (Cdh1) from the rounding cell surfaces, and the foregut does not separate into trachea and esophagus, resulting in an extended TEF. This unexpected Vangl-Celsr activity is distinct from their well-known roles in planar cell polarity (PCP), which orients cells within the plane of the epithelium. Together, these results indicate that failure to maintain localized endosome-mediated epithelial polarity during foregut morphogenesis may be a common disease mechanism underlying EA/TEF in many patients and may have broad implications for tissue fusion-fission events in the morphogenesis of other organs.

RESULTS

Mutation of endosome pathway genes discovered in EA/TEF patients causes TEFs in *Xenopus*

Recent genome sequencing of complex EA/TEF patients revealed that there is significant enrichment of potentially damaging and missense *de novo* heterozygous variants in genes involved in intracellular trafficking and endocytosis.[21] This was intriguing, considering our discovery that the recycling endosome pathway was somehow involved in tracheoesophageal morphogenesis downstream of Hedgehog signaling.[13] A meta-analysis of experimentally validated protein-protein interactions from the STRING database[22] confirmed that many proteins encoded by patient genes interact with core recycling endosome components (Figure 1A).

To systematically test the role of endosomal trafficking in EA/TEF and determine whether the patient variants were likely to be causative risk alleles, we mutated orthologous genes in *Xenopus tropicalis* using F0 CRISPR-Cas9 gene editing. We compared the resulting phenotypes to those caused by mutations in core endosome pathway genes. We designed guide RNAs (gRNAs) to create indel mutations early in the coding sequence that were predicted to disrupt protein function by creating a premature stop codon or missense mutations leading to nonsense-mediated decay.[23,24] Cas9-gRNA complexes were injected at the one-cell stage and, after 3 days of development, individual embryos were genotyped and tracheoesophageal morphogenesis was assayed by immunostaining and confocal microscopy (Figure 1B). gRNAs that reproducibly caused EA/TEF-like phenotypes with a significant penetrance compared with controls would support the patient’s variant being involved in EA/TEF. In contrast, genes that did not reproducibly cause EA/TEF when mutated in *Xenopus* were likely not disease-causing in EA/TEF patients.

Confirming the result of 10 genes previously screened,[21] as well as testing 15 additional genes, we found that mutations in 13 out of 25 orthologs of endosome-related patient risk genes result in variably penetrant tracheoesophageal anomalies in *Xenopus* (Figure 1C; Table S1). In each case, the foregut was correctly patterned into a ventral Nkx2-1+ tracheal domain and

Figure 1. Mutating EA/TEF patient endosomal trafficking genes causes TEDs in *Xenopus*

(A) STRING database interactome of endosome-related proteins with potentially pathogenic variants identified in EA/TEF patients and a curated list of core endosome pathway proteins and putative protein cargo.

(B) Experimental design of F0 CRISPR-Cas9 *X. tropicalis* mutagenesis screen to validate candidate risk genes.

(C) Confocal images of CRISPR-Cas9 *X. tropicalis* F0 mutants at NF44 stained for Sox2 (green), Foxf1 (red), and Nkx2-1 (purple). Hashed yellow lines indicate the tracheal (t) and esophageal (e) lumens. Arrows indicate TEFs. Asterisks indicate dysmorphic or occluded esophagus or trachea. Numbers indicate the proportion of mutant tadpoles with TEFs compared with the total mutants screened. Scale bars are 50 μm.

See also Figure S1 and Tables S1, S2, and S3.

a dorsal Sox2+ esophageal domain with surrounding Foxf1+ mesenchyme, and the foregut underwent initial constriction at the midline. However, in many embryos, the foregut failed to separate into distinct tubes and exhibited a persistent fistula (Figure 1C, arrows). These phenotypes were similar to those caused by mutations in the known EA/TEF risk gene *sox2*[21] and mutations in genes encoding key GTPases in endosomal trafficking: *dynamin-2* (*dnm2*), which regulates endocytosis at the cell surface, *rab5a*, which regulates early endosome vesicle trafficking, and *rab11a*,[13] involved in regulating recycling endosomes (Table S1). Mutants for some genes (*rapgef3*, *arhgap21*, *rasal2*, *ap1g2*, and *atp6v1b1*) also exhibited a dysmorphic esophagus or trachea, ranging from stenosis to a thick multilayered epithelium with multiple or occluded esophageal lumens (Figure 1C, asterisks).

Genotyping demonstrated an 80% average indel mutation rate (% alleles mutated in all genotyped cells per embryo) across all gRNAs, with a range of 58%–90% (Table S1; Figure S1A). Most gRNAs that reproducibly cause TEFs had a mutation burden exceeding 75%. Sequencing analysis revealed that a given gRNA often produced a reproducible pattern of 1–3 different mutations (Figure S1B, source data in Table S2; see STAR Methods for details on the genotype-phenotype analysis). Thus, although different cells in an embryo could have different indels, most cells likely had heterozygous or biallelic mutations. In cases when we had effective antibodies (Dnm2, Rab5a, and Rab11a), western blotting of foregut explants showed a dramatic loss of protein, and immunostaining of unilaterally injected embryos demonstrated that most of the cells (>90%) on the injected side had reduced target protein abundance (Figures S1C and S1D). Together, these data indicate that the F0 CRISPR strategy results in most embryos being more damaged than heterozygous but not complete nulls, with little cellular mosaicism.

Interestingly, in some mutants, we observed phenotypes in other tissues, including craniofacial, heart, eye, body axis, and gut coiling defects, organ systems that are also disrupted in many EA/TEF patients. However, we found no evidence of a generalized developmental delay based on developmental milestones such as melanocyte pigmentation and tail fin formation. As expected for genes in essential cellular pathways, some embryos with a very high mutation burden (>80%) exhibited gastrulation arrest and lethality before foregut morphogenesis. Taken together, these results confirm that endosomal trafficking is critical for tracheoesophageal morphogenesis in *Xenopus* and support the likelihood that variants in endosome-related genes may have caused EA/TEF in some patients.

Dynamic endosome localization and epithelial remodeling during foregut morphogenesis

To better understand the cellular mechanisms by which endosomal trafficking regulates *Xenopus* foregut morphogenesis, we performed a detailed immunostaining analysis of Dnm2, Rab5a, and Rab11a over 24 h, when the foregut separates into distinct esophageal and tracheal tubes when raised at room temperature (Figure 2).

As previously reported in Nasr et al.,[13] just before the foregut midline fuses at NF37, the endodermal tube is a typical pseudostratified columnar epithelium, with Cdh1 localized to the basal-lateral cell borders and in adherens junctions. Apical polarity proteins like aPKC and Par3 are localized to the luminal cell surface, whereas laminin (Lama1) lines the basal surface, contacting the surrounding mesoderm (Figure 2A; Figures S2A–S2C). As the foregut constricts, apical proteins aPKC and Par3 are downregulated at the midline, where the opposing epithelia touch and Tjp1+ tight junctions are lost (Figure 2B; Figures S2D–S2G). This is coincident with the localization of Cdh1 to the luminal contact surface (Figure 2B, quantification in Figure 2Q), which presumably helps mediate the adhesion of the two sides and the formation of a transient, columnar epithelial bilayer by NF39 (Figure S2J). Throughout this fusion process, all the foregut epithelial cells (dorsal, ventral, and midline) have Dnm2 detectable at the apical-lateral membrane and subapical Rab5a+ early endosome vesicles (Figures 2C–2F, quantification in Figures S2H and S2I). In contrast, Rab11a+ puncta are detectable at the apical membrane of epithelial cells in the foregut, with higher intensity levels in the midline epithelial cells (Figures 2G–2H, quantification in Figure 2Q).

12 h later, at NF41-42, cell surface Dnm2 and Rab5a+ puncta were observed throughout the epithelial bilayer, as well as in the trachea and esophageal epithelia and the surrounding mesenchyme (Figures 2K and 2M). At this point, Rab11a co-localized with Cdh1 at the adhesion surface between the two epithelial sides in the bilayer (Figures 2O–2R). As the transient bilayer began to resolve, we observed a downregulation of Rab11a and an increase in large Rab5a+ vesicles in the epithelium, consistent with elevated early endosome activity (Figures 2L, 2N, and 2P). This coincided with a loss of Cdh1 signal on cells rounding up and losing attachment to their neighbors as the mesenchyme invaded to complete separation of the foregut (Figures S2K and S2L).

Asymmetric relocalization of Cdh1 is required for trachea-esophageal separation

Our results suggested that a localized reduction in Cdh1, possibly mediated by endocytic internalization and processing to Rab5a+ early endosomes, facilitates foregut separation. To quantitatively assess Cdh1 dynamics and cell-cell contacts, we measured Cdh1 immunostaining intensity normalized to a ubiquitously expressed membrane-GFP transgene in 3D renderings of the contact surfaces between epithelial cells in the bilayer as it was separating. We found that the contact surface area between epithelial cells where the bilayer was separating was significantly smaller, with lower Cdh1 levels compared with the larger adherent surfaces of the same cells that were still in contact with adjacent esophageal and tracheal epithelia (Figures 3A and 3B). This suggests that asymmetric relocalization of Cdh1 from the rounding cell surface membrane facilitates the separation of the epithelial bilayer.

To test whether removal of Cdh1 from the cell surface by endocytosis was required for resolution of the bilayer, we expressed a Cdh1 mutant (ΔLL-Cdh1) that cannot be internalized by clathrin-dependent endocytosis[25] using *Xenopus* F0 transgenesis (Figure 3C). The bipartite transgene *Tg(hhex:trTA; TRE:ΔLL-Cdh1-GFP)* specifically expresses the mutant ΔLL-Cdh1 or a control wild-type (WT)-Cdh1 in the foregut upon administration of doxycycline (DOX). Compared with non-induced and WT-Cdh1 controls, approximately 70% of ΔLL-Cdh1 transgenic embryos exhibited a TEF, with a significantly

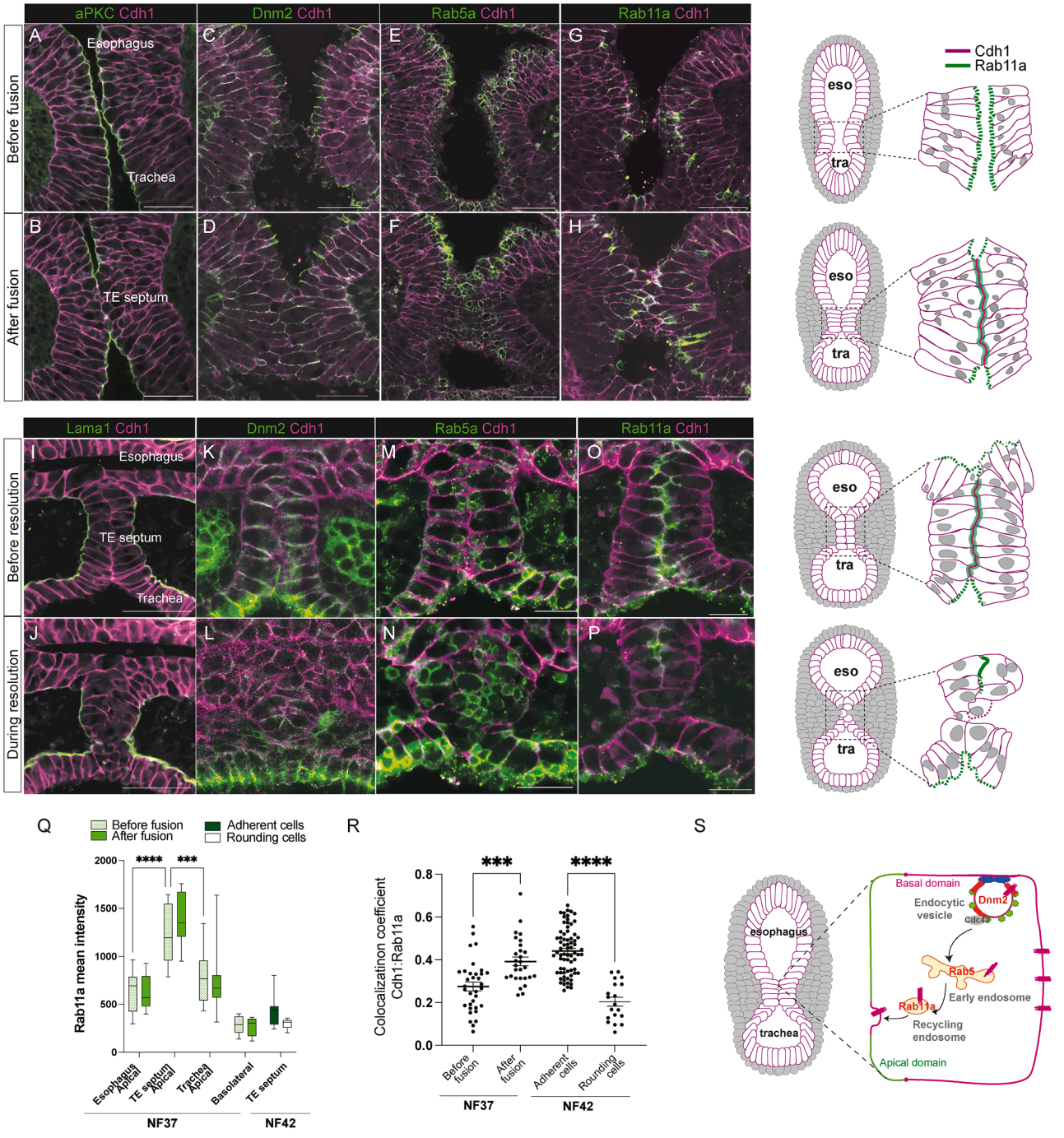

Figure 2. Dynamic endosome localization and epithelial remodeling during tracheoesophageal morphogenesis

(A–B and I–J) Immunostaining of aPKC, laminin (Lama1), and Cdh1 dynamics in the *Xenopus* foregut during trachea-esophageal morphogenesis. Scale bars, 50 μm.

(C–H and K–P) Immunostaining of Dnm2, Rab5a, and Rab11a in the *Xenopus* foregut during trachea-esophageal morphogenesis. Scale bar, 50 μm. Diagrams depict the temporospatial dynamics of Cdh1 and Rab11a subcellular localization during tracheoesophageal morphogenesis.

(Q) Quantification of Rab11a immunostaining intensity during foregut fusion and separation (mean ± min/max, 2W-ANOVA, ****$p < 0.0001$, n = 4–6 embryos analyzed).

(R) Cdh1-Rab11a co-localization at the epithelial interface (mean Pearson co-localization coefficient ± SEM, *** $p < 0.001$, **** $p < 0.0001$ 1W-ANOVA, n = 5–13 cells per embryo, N = 6–8 embryos per stage).

(S) A model of how endosomal trafficking may mediate Cdh1 relocalization during epithelial fusion.

See also Figure S2.

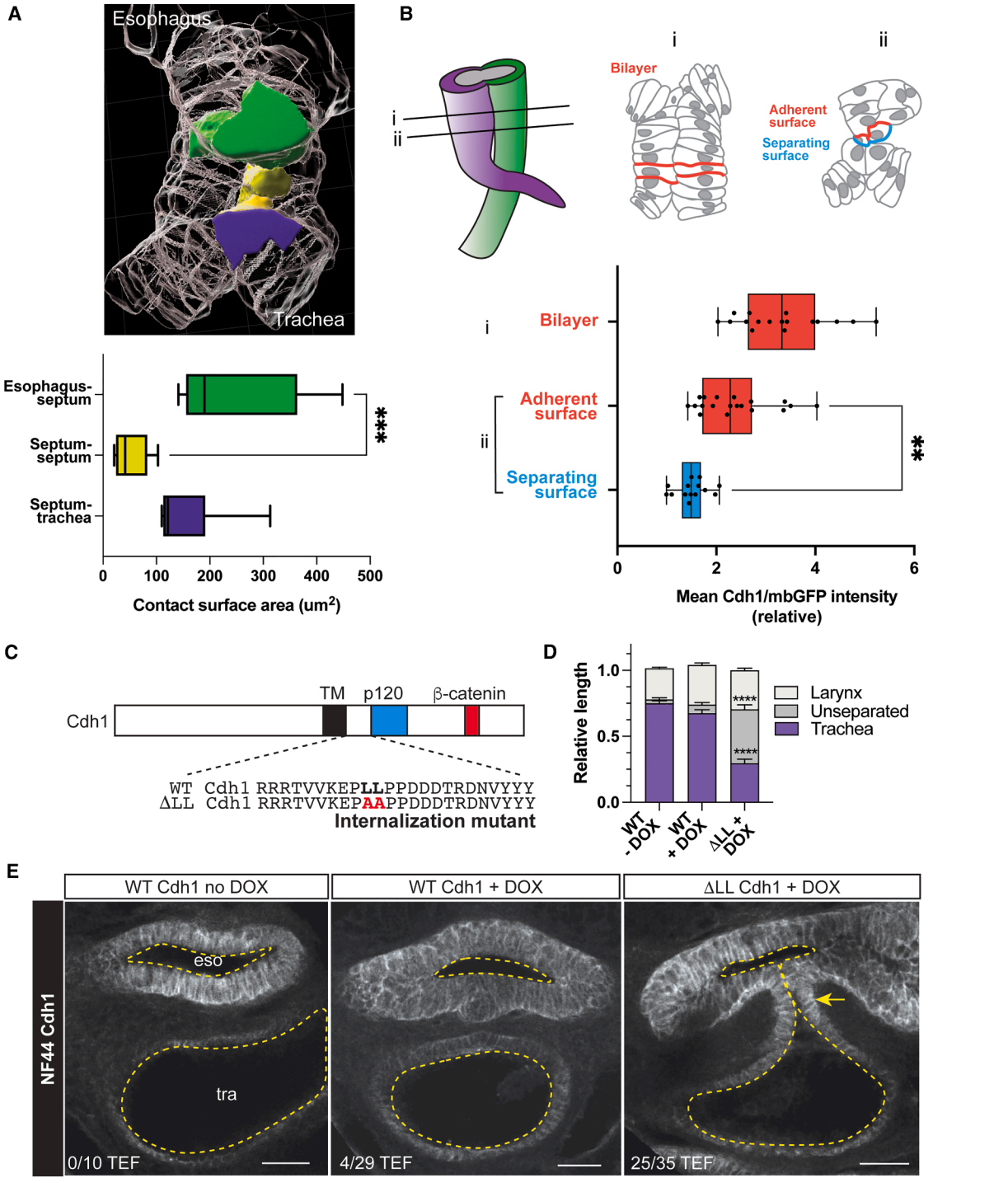

Figure 3. Endocytosis of Cdh1 is required for trachea-esophageal separation

(A) 3D cell-surface rendering of the resolving septum with esophageal cells in green, septal cells in yellow, and tracheal cells in purple. Septal cells significantly decrease surface contact area with each other compared with the contact between tracheal cells and esophageal cells (mean ± min/max, *** $p < 0.001$ 1W-ANOVA, $n = 6$ cells per embryo, $N = 9$ embryos).

(B) Diagrams of the separating foregut at i) the intact bilayer and ii) at the point where the bilayer is separating. The graph quantifies Cdh1/mbGFP intensity at cell surfaces in the bilayer and the adherent vs. separating side of the cells losing contact (mean ± min/max, ** $p < 0.01$ 1W-ANOVA, $n = 5$ cells per embryo, N=6 embryos).

(legend continued on next page)

longer segment of unseparated epithelial bilayer (Figures 3D and 3E). This demonstrates that endocytosis of Cdh1 is required for the epithelial bilayer to undergo fission and separate the trachea and esophagus.

Endosomal trafficking is required for maintenance and resolution of the epithelial bilayer during tracheoesophageal morphogenesis

Next, we determined which epithelial remodeling events driving tracheoesophageal morphogenesis require endosomal trafficking. Surprisingly, initial foregut constriction and epithelial fusion, with downregulation of aPKC and increased localization of Cdh1 at the contact surface, occurred normally in *dnm2*, *rab5a*, and *rab11a* mutant embryos (Figure 4A). The earliest cellular phenotype we observed was a disorganized septum 4–6 cells wide, with cells in the middle being round rather than the stereotypical columnar epithelial bilayer at NF41 (Figure 4B, quantified in Figure 4E). Moreover, at NF42, when the septum in control embryos is separating, the mutant septum did not downregulate Cdh1 and resolve into the distinct trachea and esophageal tubes. Rather, a disorganized epithelial mass persisted, resulting in a blind-ended fistula (Figures 4C and 4D; Table S1). Interestingly, we frequently observed blisters in the endosome mutant septa, which exhibited asymmetric reductions in Cdh1 on the luminal surface, suggesting that some cells in the tissue try to separate from one another, but other cell-cell contacts prevent complete septation (Figure 4D). Occasionally, the endosomal mutants also exhibited a dysmorphic esophagus and occluded tracheal lumens (Figure 4B; Table 1). These results indicate that endosomal trafficking is required to maintain an organized epithelial bilayer and suggest that the accumulation of too many cells with persistent Cdh1 at epithelial-epithelial interfaces disrupts the resolution into distinct trachea and esophageal tubes.

To determine whether the accumulation of cells was due to elevated cell proliferation, we quantified confocal z stack of the entire foregut region. We found that neither the total number of cells in the trachea-esophageal septum nor the rate of proliferation (phosphorylated histone H3 staining) was significantly increased in endosomal mutants compared with controls (Figures 4F and 4G). Three-dimensional reconstructions demonstrated that the mutant septa were wider (x axis) and shorter in the rostral-caudal axis (z axis) compared with controls but were similar in the dorsal-ventral axis (y axis) (Figure S3). This indicates that mutant cells somehow accumulate across the width of the epithelial septum at the expense of fewer cells along the rostral-caudal extension of the separating trachea and esophagus.

Endosomal trafficking controls the orientation of division in the foregut epithelial bilayer

The earliest cellular phenotype we observed in endosome CRISPR mutants was the significant accumulation of cells inside the epithelial bilayer after foregut fusion. Because cells in pseudostratified and columnar epithelia are known to divide into the plane of the tissue to maintain appropriate organization, we considered the possibility that, in the mutant embryos, cells might aberrantly divide into the middle of the septum, contributing to the cell buildup (Figure 5A). To assess the plane of cell division, we measured the angle of the mitotic spindle relative to the basal membrane in the septum of endosomal mutants and controls. Whereas cells in the epithelial bilayer of control embryos divided into the plane of the epithelia as expected, with an average spindle orientation of 0–15°, *dnm2*, *rab5a*, and *rab11a* mutants exhibited a more random distribution of mitotic spindle angles (Figures 5B and 5C). This defect was primarily localized to the septum, as the mitotic spindle angles in the trachea and esophagus were not significantly different between mutants and controls (Figure S4). Thus, loss of endosomal trafficking causes aberrant cell division into the center of the epithelial bilayer and possibly a defect in reintegration into the epithelial tissue after cell division due to altered apical-basal cell polarity. To test whether these changes in the orientation of cell division were linked to altered apical-basal cell polarity, we performed immunostaining for laminin, which is usually secreted from the basal side of epithelia into the extracellular matrix. We observed that mutant embryos exhibited ectopic laminin deposition in the center of the disorganized septum surrounding the round central cells and in the lumens of blisters within the tissue (Figures 5D–5G). These observations are consistent with disrupted endosomal trafficking leading to loss of apical-basal polarity in the transient epithelial bilayer, randomized cell division, and cells accumulating in the mutant tracheoesophageal septum.

Endosomal trafficking localizes Vangl2 to maintain apical memory in the epithelial bilayer

During foregut morphogenesis, when the apical epithelial cell surfaces from either side touch one another, they lose apical markers (aPKC and Par3) and gain Cdh1 (typically basal-lateral) as they adhere and form the transient bilayer. Despite this apparent loss of apical identity, the cells must somehow retain some apical-basal information to form an organized bilayer and undergo cell division in the plane of the epithelium—a process that we found requires endosomal trafficking. One candidate pathway that might regulate this process is the Vangl-Celsr polarity complex. In addition to their well-known role in the Wnt/PCP pathway, where heterotypic cell-cell interactions between transmembrane Vangl, Celsr, and Frizzled proteins govern cell orientation in the plane of the epithelia,[26] Vangl and Celsr are also involved in specifying apical-basal polarity in epithelia by recruiting apical Par3 and aPKC while restricting Scrib to the basolateral domain.[16,27,28] Furthermore, apical Vangl-Celsr complexes are reported to be internalized by endosomes during polarized cell divisions of the fetal mouse epidermis,[29] suggesting a potential mechanistic link in the foregut.

To assess whether Vangl-Celsr complexes are involved in endosome-dependent epithelial remodeling in the foregut, we

(C) Structure of wild-type (WT) and the ΔLL → AA Cdh1 mutant that cannot be internalized by endocytosis.[25]
(D) Quantification of the TEF phenotype in ΔLL-Cdh1 mutants compared with WT-Cdh1 and no DOX control embryos (mean ± SEM, ****$p < 0.0001$ 1W-ANOVA, $n = 10–35$ embryos from 3 transgenesis experiments).
(E) Cdh1 immunostaining and confocal microscopy of NF44 transgenic embryos and controls. Scale bars, 50 μm.

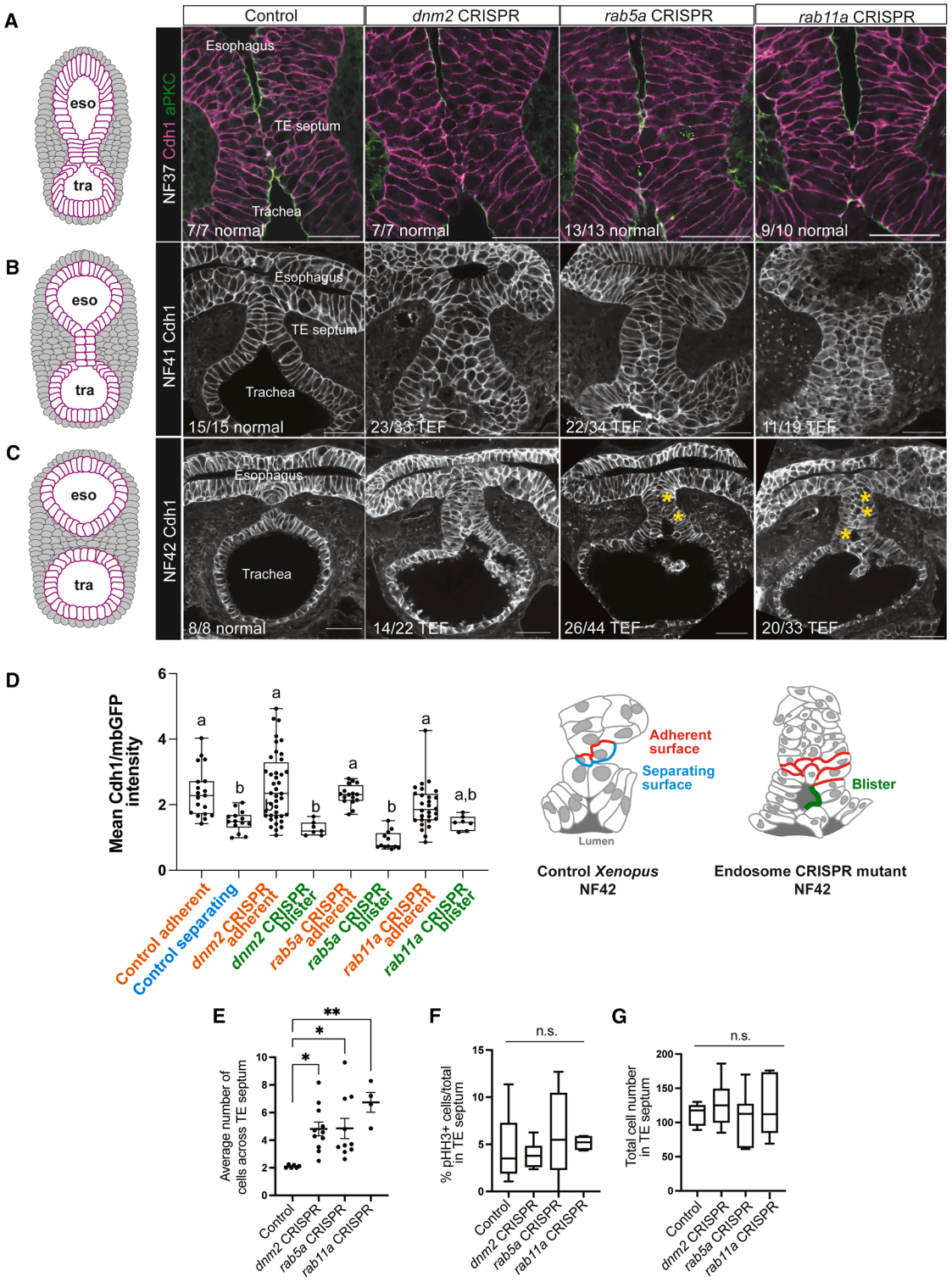

Figure 4. Endosomal trafficking is required for resolution of the epithelial bilayer

(A) At NF37, the septum in *dnm2*, *rab5a*, and *rab11a* CRISPR mutants undergoes epithelial fusion similar to controls. Scale bars, 50 μm.

(B) At NF41, the epithelial bilayer in endosomal mutants is disorganized compared with controls. Scale bars, 50 μm.

(C) *dnm2*, *rab5a*, and *rab11a* CRISPR mutants exhibit TEFs and blisters in the TE septum (asterisks). Scale bars, 50 μm.

(legend continued on next page)

performed Vangl2 and Celsr1 immunostaining in combination with Rab11a (effective antibodies are not available for *Xenopus* Celsr2 and Vangl1). Before foregut fusion, diffuse Vangl2 was observed throughout the foregut epithelia, with no apparent difference between apical and basolateral cell domains (Figures 6A–6F). However, as the midline epithelia touched, Vangl2 became progressively co-localized with Rab11a puncta at the luminal/apical contact point and subsequent adherent interface of the bilayer (Figure 6; Figure S5). Super-resolution microscopy demonstrated that approximately 40% of Rab11a and Vangl2 puncta at the adherent interface of the bilayer were within 500 nM of each other, consistent with the size of a recycling endosome vesicle.[30,31] In contrast to this dynamic Vangl2 subcellular localization, Celsr1 remained around the entire juxta-membrane region of the epithelial bilayer cells throughout tracheoesophageal morphogenesis (Figures S5E–S5H).

Considering that endosomes are reported to internalize cell surface Vangl2 in the fetal mouse epidermis,[26] this suggested that Vangl2 might be a cargo of the Rab11+ recycling endosomes, transporting it to the cell surface where the epithelia fuse. To test this possibility, we examined Vangl2 localization in the endosomal mutants. Vangl2-Rab11a co-localization at the epithelia contact was lost in the disorganized multilayer septum of *dnm2*, *rab5a*, and *rab11a* mutants (Figures 6J–6N; Figure S5D). However, Celsr1 localization and apical Vangl2 in the esophagus and trachea were unaffected (Figures 6K–6M, asterisks; Figures S5I–S5M), indicating that recycling endosomes are required to localize Vangl2 at the midline apical interface.

Mutation of EA/TEF patient-like genes in *Xenopus* disrupts Rab11-Vangl2 localization

We next assessed whether a similar mechanism was involved in the TEFs observed when we mutated the *Xenopus* orthologs of endosome pathway risk genes from patients. These included *AP3D1*, *ARHGAP21*, and *ITSN1*, which encode endocytic vesicle adaptor proteins and CDC42-GEFs, as well as *ATP6V1B1*, which encodes a vacuolar ATPase subunit required for acidification of endosomal vesicles.[32–36] As predicted, F0 CRISPR mutants of *ap3d1*, *arhgap21*, *atp6v1b1l,* and *itsn1* all exhibited a loss of apical Vangl2 localization and a disorganized persistent septum (Figures 6O–6R), consistent with these proteins functioning upstream of Rab11 in the recycling endosome pathway.

Together, these results indicate that during tracheoesophageal morphogenesis, dynamic recycling endosome activity is required to localize Vangl2 at the cell surface, where the opposing midline epithelia adhere to one another. Vangl2 appears to define an ‘‘apical memory’’ in the epithelial bilayer cells that have lost aPKC and upregulate cadherin, a membrane configuration more typical of adherent basal-lateral cell-cell contacts. This unexpected behavior is distinct from the typical roles for Vangl2 in apical-basal and planar cell polarity.

Loss of Vangl or Celsr disrupts tracheoesophageal morphogenesis, resulting in TEFs

The results above imply that Vangl-Celsr is required for tracheoesophageal morphogenesis. Interestingly, one patient from our EA/TEF cohort had a heterozygous *de novo* damaging missense variant in *CELSR2* predicted to alter an amino acid (N953S) in an N-terminal cadherin domain.[21,37] Moreover, a rare *de novo* variant in CELSR1 (V1452I) was previously reported in another EA/TEF patient.[38] Together with our observations that cell polarity is disrupted in endosomal mutants, this led us to test whether Vangl-Celsr were required for trachea-esophageal morphogenesis in *Xenopus*.

Loss-of-function CRISPR-Cas9 F0 *Xenopus* mutants for *celsr2*, *celsr1*, or *vangl2* all resulted in variably penetrant TEFs in 25%–30% of the embryos at NF44 (Table 1). Examination of the mutant foreguts at NF40 revealed a disorganized, thicker septum with round cells in the middle and frequent blisters, phenocopying the endosomal mutants (Figures 7A–7D). Moreover, the *celsr1* and *celsr2* mutants exhibited reduced Vangl2 immunostaining, consistent with previous reports that Celsr1 forms a heterotypic cell-cell complex with Vangl2.[26] Interestingly, in *vangl2* and *celsr1/2* mutants, Rab11a was still localized to the middle of the bilayer (Figures 7E–7H), indicating that Vangl-Celsr complexes are required for tracheoesophageal morphogenesis downstream of recycling endosomes. Together, these results suggest that an unexpected but evolutionarily conserved endosome-cell polarity pathway controls tracheoesophageal morphogenesis and that disruptions to this process might contribute to EA/TEF in many patients (Figure 7I).

DISCUSSION

In this study, we demonstrate that an endosome-cell polarity pathway is required for the epithelial remodeling that drives *Xenopus* tracheoesophageal morphogenesis. We discovered that Rab11+ recycling endosomes localize the transmembrane polarity protein Vangl2 to the contact surface where foregut epithelia fuse. This appears to confer an ‘‘apical memory,’’ which is essential to maintain an organized transient epithelial bilayer and its subsequent fission into distinct trachea and esophagus (Figure 7I). This unexpected Rab11-Vangl2 activity is distinct from its typical roles in planar cell polarity and apical basal polarity and may represent a general paradigm for epithelial fusion and fission during morphogenesis.

Our study provides insight into how cell and tissue polarity is dynamically regulated during tissue fusion and fission through the physical relocation of polarity proteins in cells by endosomal trafficking pathways. Previous work suggests that the hierarchy of endosomal trafficking and cell polarity in development is context dependent. Endosomes internalize planar-cell-polarized Vangl, Celsr, and Fzd proteins in the fetal mouse epidermis, which are later relocated back to the appropriate cell surface

(D) Quantification of Cdh1/mbGFP intensity in the adherent, separating, and luminal cell surfaces in control septal and endosomal mutant blisters (mean ± min/max, 1W-ANOVA, different letters indicate $p < 0.05$ between groups, $n = 7–40$ cells, $N = 3–5$ embryos)
(E) The NF41 mutant septa have more cells across the width compared with controls (mean ± SEM, * $p < 0.05$ 1W-ANOVA, ** $p < 0.01$, $N = 6–11$ embryos).
(F and G) (F) There are no significant (n.s.) differences in proliferation (pHH3+/total) or (G) total cells in the septum of mutant embryos compared with controls (mean ± min/max, 1W-ANOVA, $N = 46$ embryos).
See also Figure S3.

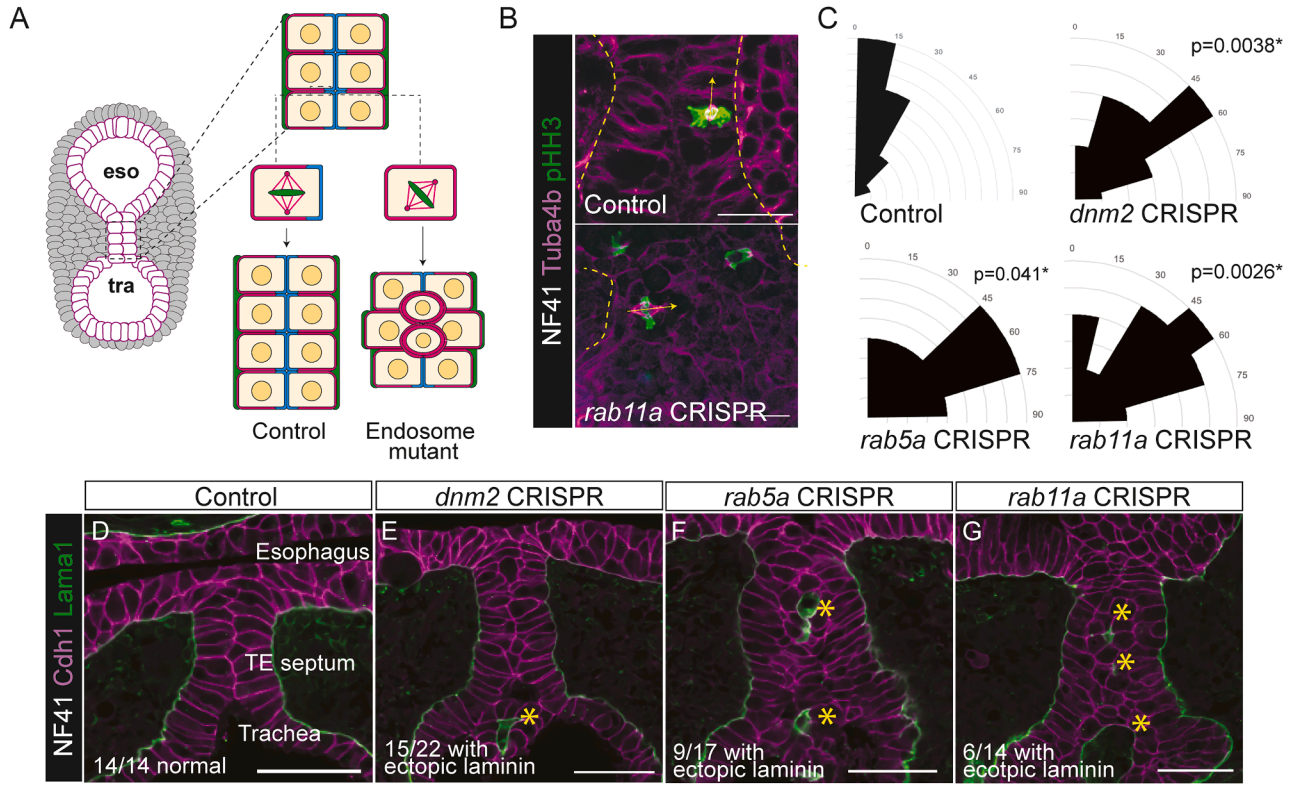

Figure 5. Endosomal trafficking controls the polarity of epithelial cell division

(A) A model of altered cell division orientation in endosomal mutants causing cells to accumulate in the epithelial septum.

(B) Immunostaining of the mitotic spindle (Tuba4a and phospho-histone H3) was used to measure the angle of cell division. Scale bars, 50 μm.

(C) Distribution of mitotic spindle angles is random in endosomal mutant epithelial cells compared with controls, which consistently divide between 0° and 15° (n = 3–15 spindles per embryo, Kolmogorov-Smirnov test, N = 4–6 embryos.

(D–G) Endosomal mutants have ectopic laminin deposits (asterisks) inside the blistered disorganized epithelia. Scale bars, 50 μm.

See also Figure S4.

after cell division to maintain epithelial organization.[29] In contrast, Vangl2 functions upstream of Rab11 in classical Wnt/PCP and apical-basal polarity roles to regulate convergent extension, planar cell polarization, and apical constriction during Xenopus gastrulation and neural tube morphogenesis.[39–41] We show in the foregut that Rab11a is upstream of Vangl2, as Rab11a is still localized properly in *vangl/celsr* F0 CRISPR mutants. Endosomal trafficking mechanisms to internalize and replace polarity proteins during cell division might explain the maintenance of polarized cell division in the transient epithelial bilayer of the foregut, but, in the mouse epidermis, this is a classical polarized epithelium, and, in the foregut, we propose Vangl2 confers "apical memory" to cells that have otherwise lost apical character independent of planar cell polarity signaling. Another distinction between what we have described in the foregut and these other examples of Vangl-regulated epithelial polarity in morphogenesis is that in the foregut the epithelia first fuse (like the neural tube and palate) but then undergo fission. Other tissues that experience this type of dynamic fusion-fission morphogenesis include separation of anorectal tubes in the hindgut and semicircular canals in the ear.[42–44] We predict that similar Rab11a-Vangl2 mechanisms may act in those tissues.

We also show a role for Vangl2 in maintaining tissue polarity cues distinct from its typical functions in planar cell and apical-basal cell polarity mechanisms. Our observation that Vangl2 and Rab11a co-localize coincident with a loss of Par3 and aPKC in the foregut bilayer epithelium was unexpected because Vangl2 is typically thought to help recruit these proteins to the apical surface in a polarized epithelium. Vangl2 has previously been implicated in developmental processes independent of its classical polarity roles. In the developing mouse pancreas, apical restriction of Vangl2 maintains epithelial integrity independent of apical-basal cell polarity.[45] Vangl2 has cell shape and polarity functions in the developing mouse lung mesenchyme during branching morphogenesis independent of its planar cell polarity roles.[46,47] Neither the *looptail* mutation (dominant negative) nor conditional knockout of Vangl2 using ShhCre impairs trachea-esophageal separation; however, a different Cre driver with earlier recombination in the foregut might lead to separation anomalies. The observation that endosomal and polarity (*vangl2* and *celsr1/2*) Xenopus CRISPR mutants in our study do not have 100% penetrance of EA/TEF suggests there may be genetic redundancy between *rab11* (*rab11a* vs. *rab11b*) and *vangl* family members (*vangl1* vs. *vangl2*). Redundancy between *Rab11a/b* was shown in the developing mouse pancreas, as knockout of both *Rab11a* and *Rab11b* was required to see epithelial defects.[48] Another possibility is that there are other cargo proteins necessary to maintain epithelial organization in the foregut,

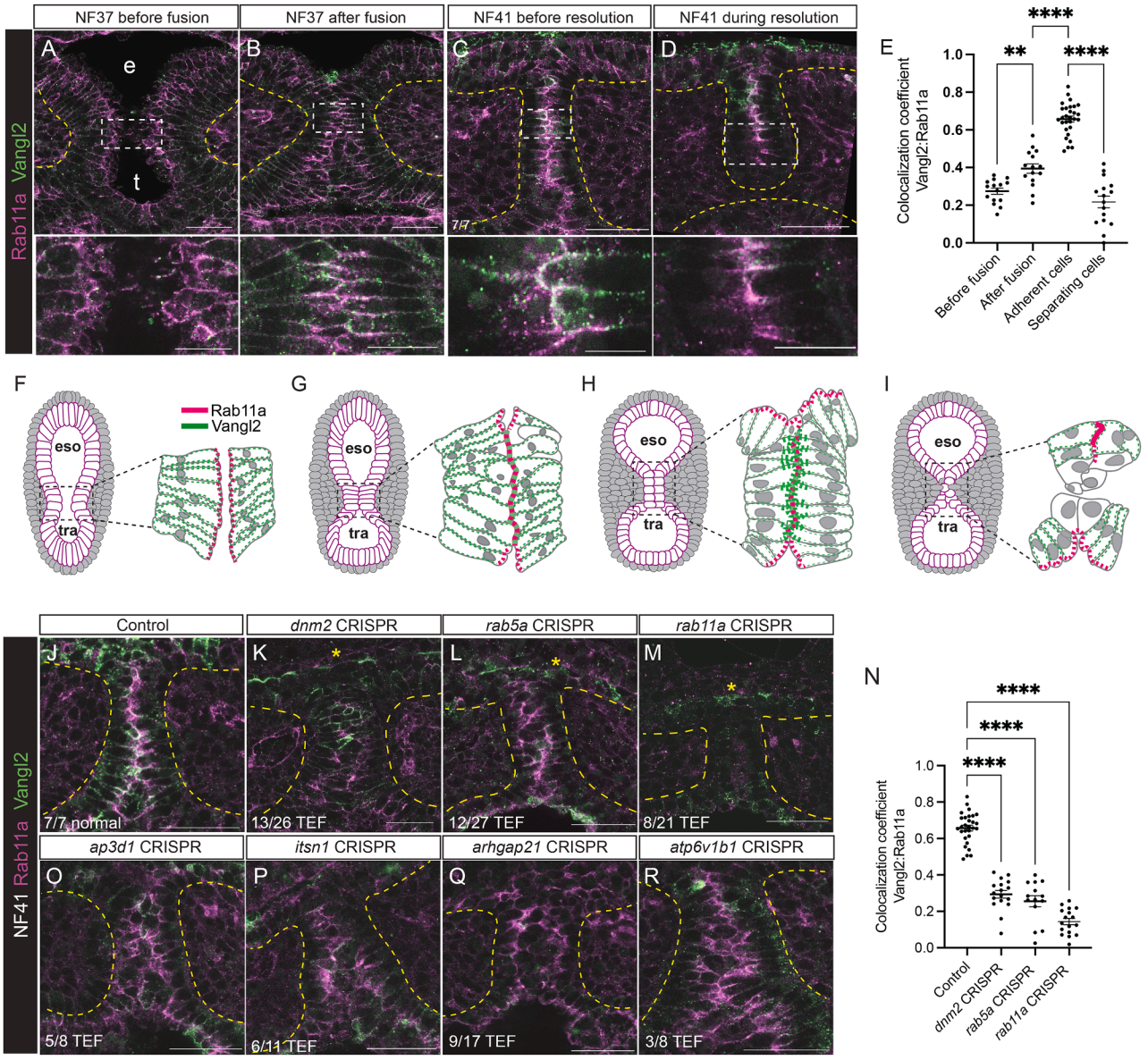

Figure 6. Recycling endosomes localize Vangl2 to maintain apical memory in the transient trachea-esophageal septum

(A–D) Time course of Vangl2-Rab11a immunostaining during *Xenopus* tracheoesophageal separation. Scale bars, 50 μm and 20 μm (inset).

(E) Dynamic Vangl2-Rab11a co-localization at the epithelial interface (mean Pearson co-localization coefficient ± SEM, *** $p < 0.001$, **** $p < 0.0001$ 1W-ANOVA, $n = 6$ cells per embryo, $N = 5$ embryos per stage).

(F–I) Diagrams of Vangl2-Rab11a localization during foregut separation.

(J–M) Vangl2 is mis-localized in septal epithelial cells of endosomal mutants.

(N) Endosomal mutant septa have significantly lower Vangl2-Rab11a co-localization relative to controls (mean ± SEM, **** $p < 0.0001$ 1W-ANOVA, $n = 5$ cells per embryo, $N = 4$–6 embryos per condition).

(O–R) CRISPR F0 mutation of patient variant orthologous genes in *Xenopus* (*ap3d1*, *itsn1*, *arhgap21*, and *atp6v1b1*) disrupts Vangl2 localization in the TE septum. Scale bars are 50 μm (20 μm in insets).

See also Figure S5.

explaining why loss of Vangl2 is only ~30% penetrant for an EA/TEF phenotype.

Our data, together with previously published work, suggest that Vangl2—and possibly Cdh1 (E-cadherin)—is a cargo of recycling endosomes. Unlike Vangl2, Cdh1 does not require recycling endosomes to localize to the midline of the fused epithelial bilayer. However, we show that Cdh1 needs to be internalized by endocytosis at the separating epithelial cell surface for fission of the bilayer into the trachea and esophagus. We postulate that other endosomal cargo may include integrins that facilitate tissue adhesion and laminins that mediate interaction with the adjacent mesoderm at the basal surface. Consistent with this

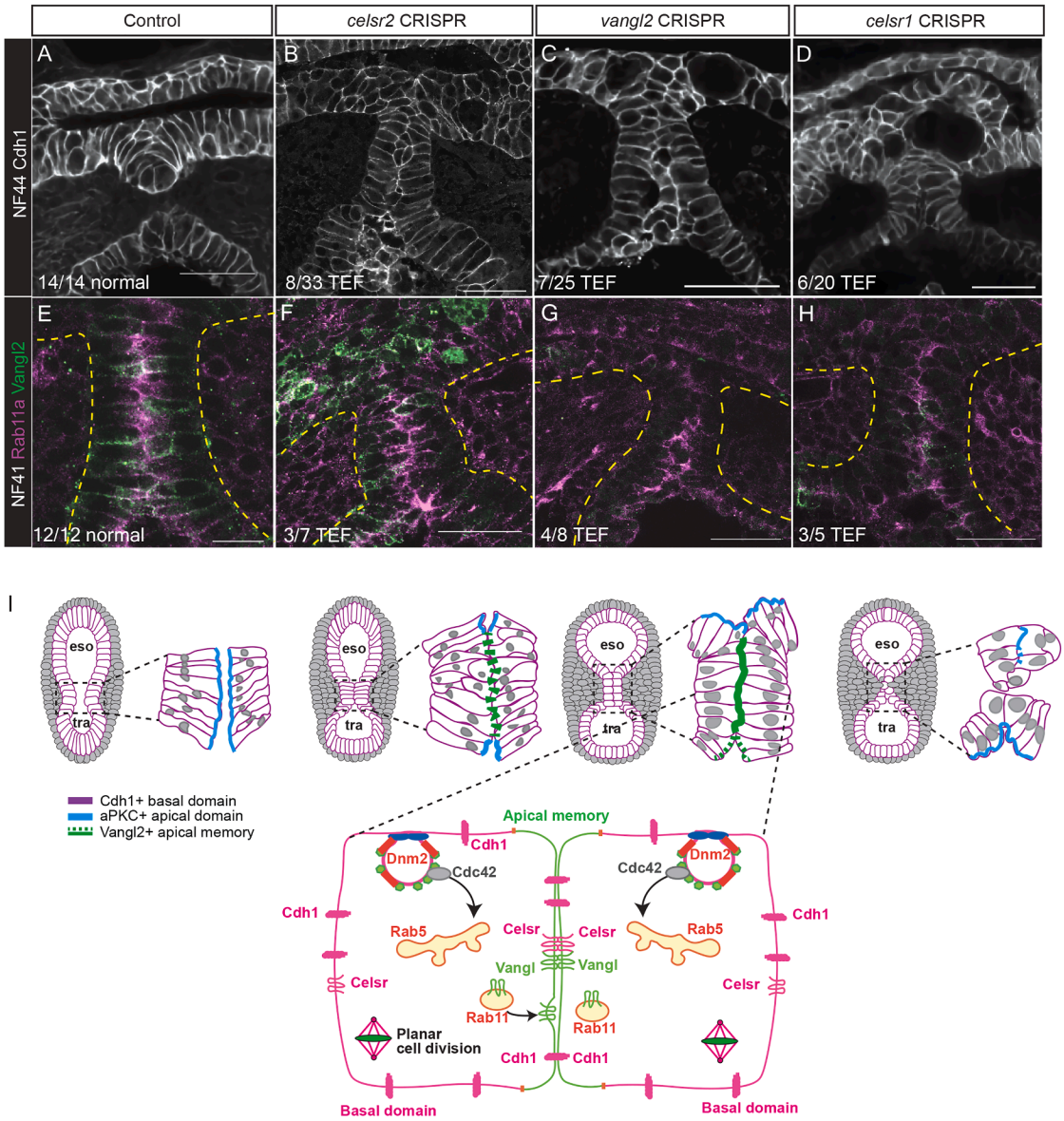

Figure 7. Loss of Vangl or Celsr disrupts tracheoesophageal morphogenesis, resulting in TEFs

(A–D) Cdh1 immunostaining in *celsr2*, *vangl2*, and *celsr1* mutants with TEFs. Scale bars, 50 μm.

(E–H) Disorganized epithelial septa that fail to co-localize Vangl2-Rab11a. Scale bars, 50 μm.

(I) Model of how endosomal trafficking of Vangl2 maintains apical-basal polarity information and tissue organization required for tracheoesophageal morphogenesis.

possibility, we note that EA/TEF patients were identified with potentially damaging variants in *ITGB4* and *LAMB4*.[21] Another candidate pathway that might regulate endosome-mediated loss of adhesion is the Eph/ephrin pathway. Eph/ephrins are known to regulate tissue separation and cell sorting in many contexts[49] and *Efnb2* was recently shown to be required for trachea-esophageal separation downstream of Nkx2-1.[50,51] In the future, we will test the intriguing possibility that ephrin-cadherin-endosome-Vangl interactions mediate tissue adhesion and separation in the developing foregut.

Endosomal trafficking is a ubiquitous cell pathway required for homeostasis and many basic cellular functions. Several pleiotropic diseases are associated with variants in endosomal trafficking genes,[20] but, interestingly, many of these are rather specific to certain tissues. Not surprisingly, total loss of endosome activity leads to early embryonic lethality in germline mutant mice[52,53] and in *Xenopus* embryos results in gastrulation and neurulation defects.[39] Our F0 CRISPR mutagenesis on the other hand results in 58%–90% indel mutations, more damaged than a heterozygote but not complete nulls. Indeed, in our experiments, endosomal mutant embryos have a significantly higher frequency of gastrulation and neurulation defects compared with controls where the pigmentation genes *tyr* and *slc45a2* were mutated. In our experiments, we selected those embryos that

survived to later stages. The fact that later embryos with partial loss of endosome activity show specific defects suggests that developing organs and tissue undergoing dynamic epithelial remodeling, like tracheoesophageal separation, represent developmental bottlenecks that are particularly sensitive to disruptions in endosomal trafficking. This may partially explain why EA/TEF patients frequently present with variants predicted to have partial loss-of-function or hypomorphic variants in endosome and polarity pathway genes.

Our results support the "saddle rising" model of tracheaesophageal separation and provide a cellular basis for the saddle as the point of epithelial fusion-fission and mesenchymal invasion. We note differences between Xenopus and mouse TE morphology and anatomy—in mice, the epithelial fusion event is more transient and only 3–4 cells in length, whereas in Xenopus, the epithelial fusion event is more prolonged, forming a bilayer septal tissue over 10 cells in length. In mammals the foregut tissue significantly grows in the longitudinal plane as the trachea and esophagus separate, resulting in an apparent "rising" of the saddle compared with Xenopus. Our study uses Xenopus as a model to perform rapid disease causality screening and cellular analysis to minimize the confounding issue of tissue growth.

The EA/TEF risk genes that we validated in this study are predicted to function at various levels of endosomal trafficking pathways, including formation of an endocytic vesicle (*ITSN1* and *AP1G2*), cytoskeletal transport (*ARHGAP21*, *ABRA*, *RASAL2*, and *RAPGEF3*), and endosomal acidification (*ATP6V1B1*). We also discovered that variants in *CELSR1/2*, including a damaging missense variant in *CELSR2* in a patient from this cohort, are implicated in EA/TEF and other foregut anomalies.[21,38] Furthermore, variants in *VANGL1/2* underlie a broad spectrum of developmental anomalies in humans,[26] such as neural tube anomalies,[54,55] renal anomalies,[56,57] congenital heart anomalies,[58,59] and lung diseases,[60] and may be trafficked by endosomes to specific cellular domains during development of these organs. Complex EA/TEF patients tend to have comorbidities in these same organs that experience tissue fusion events during fetal development.[21] This suggests that disruption of a conserved endosome-polarity pathway may account for pleiotropic phenotypes in many complex EA/TEF patients. Together, this suggests the provocative possibility of an endosomeopathy developmental syndrome, akin to ciliopathies. Further comparative analysis of patient genetics and animal models will improve our understanding of fundamental tissue fusion and fission events in development and advance our knowledge of the developmental basis of congenital anomalies, informing the care and treatment of endosomeopathy patients.

Limitations of the study

The F0 CRISPR-Cas9 gene editing strategy used in our study is inherently variable compared with analyzing germline mutants. We took advantage of rapid *Xenopus* embryonic development to efficiently screen patient risk genes generating simple indels that produced loss-of-function mutations. However, it is possible that variants in EA/TEF patients instead generate gain of function or hypomorphic protein products. To better understand genotype-phenotype causation, future studies should model the precise patient variant in *Xenopus* using homology-directed repair CRISPR strategies. We also do not rule out the possibility that endosomal trafficking is required in surrounding mesenchymal cells to secrete matrix metalloproteases for basement membrane degradation and for directional migration of the mesenchyme to populate the midline during trachea-esophageal separation. Because our gene editing strategy targeted both epithelial and mesenchymal tissues in this study, these questions can be tested in follow-up studies using tissue-specific manipulations in *Xenopus* or mouse.

RESOURCE AVAILABILITY

Lead contact

Requests for further information and resources should be directed to, and will be fulfilled by, the lead contact, Aaron Zorn (aaron.zorn@cchmc.org).

Materials availability

All unique reagents generated in this study are available from the lead contact upon request.

Data and code availability

Any additional information required to reanalyze the data reported in this paper is available from the lead contact upon request.

ACKNOWLEDGMENTS

We thank the Bio-Imaging and Analysis Facility for imaging and analysis advice (RRID: SCR_022628) and the Division of Veterinary Services and the DNA Sequencing Core at CCHMC (RRID: SCR_022630) for their services used in this study. We thank Sergei Sokol for kindly providing the anti-Vangl2 antibody. We are grateful to the NIH-funded National Xenopus Resourse (RRID: SCR_013731) and Xenbase (RRID: SCR_003280) for public support of *Xenopus* research. We thank the members of the CLEARconsortium.org for access to EA/TEF patient data and for helpful discussions. This work is supported by NICHD P01HD093393 to Y.S., W.K.C., and A.M.Z. and a Canadian Institutes of Health Research postdoctoral fellowship to N.A.E.

AUTHOR CONTRIBUTIONS

Conceptualization: N.A.E. and A.M.Z. Formal analysis: N.A.E., A.K., and A.M.Z. Funding acquisition: Y.S., W.K.C., and A.M.Z. Investigation: N.A.E., S.A.R., A.K., A.W., Z.N.A., and A.P.K. Methodology: N.A.E., S.A.R., and M.K. Project administration: N.A.E. and A.M.Z. Supervision: N.A.E. and A.M.Z. Validation: N.A.E. Visualization: N.A.E. and A.M.Z. Writing – original draft: N.A.E. and A.M.Z. Writing – review & editing: all authors.

DECLARATION OF INTERESTS

The authors declare no competing interests.

STAR★METHODS

Detailed methods are provided in the online version of this paper and include the following:

- KEY RESOURCES TABLE
- EXPERIMENTAL MODEL AND STUDY PARTICIPANT DETAILS
  - CRISPR-Cas9 gene editing and Xenopus embryo culture
  - Genotype-phenotype scoring
  - E-Cadherin (Cdh1) site-directed mutagenesis and *Xenopus* transgenesis
- METHOD DETAILS
  - Whole mount immunostaining and confocal microscopy
  - Image analyses
  - Immunoblotting
- QUANTIFICATION AND STATISTICAL ANALYSIS

SUPPLEMENTAL INFORMATION

Supplemental information can be found online at https://doi.org/10.1016/j.devcel.2025.04.026.

Received: November 21, 2023
Revised: December 18, 2024
Accepted: April 29, 2025
Published: May 23, 2025

REFERENCES

1. Edwards, N.A., Shacham-Silverberg, V., Weitz, L., Kingma, P.S., Shen, Y., Wells, J.M., Chung, W.K., and Zorn, A.M. (2021). Developmental basis of trachea-esophageal birth defects. Dev. Biol. *477*, 85–97. https://doi.org/10.1016/j.ydbio.2021.05.015.
2. Raad, S., David, A., Que, J., and Faure, C. (2020). Genetic Mouse Models and Induced Pluripotent Stem Cells for Studying Tracheal-Esophageal Separation and Esophageal Development. Stem Cells Dev. *29*, 953–966. https://doi.org/10.1089/scd.2020.0075.
3. van Lennep, M., Singendonk, M.M.J., Dall'Oglio, L., Gottrand, F., Krishnan, U., Terheggen-Lagro, S.W.J., Omari, T.I., Benninga, M.A., and van Wijk, M.P. (2019). Oesophageal atresia. Nat. Rev. Dis. Primers *5*, 26. https://doi.org/10.1038/s41572-019-0077-0.
4. Chitkara, A.E., Tadros, M., Kim, H.J., and Harley, E.H. (2003). Complete laryngotracheoesophageal cleft: complicated management issues. Laryngoscope *113*, 1314–1320. https://doi.org/10.1097/00005537-200308000-00010.
5. Bednarczyk, D., Sasiadek, M.M., and Smigiel, R. (2013). Chromosome aberrations and gene mutations in patients with esophageal atresia. J. Pediatr. Gastroenterol. Nutr. *57*, 688–693. https://doi.org/10.1097/MPG.0b013e3182a373dc.
6. Stoll, C., Alembik, Y., Dott, B., and Roth, M.P. (2017). Associated anomalies in cases with esophageal atresia. Am. J. Med. Genet. A *173*, 2139–2157. https://doi.org/10.1002/ajmg.a.38303.
7. Brosens, E., Ploeg, M., van Bever, Y., Koopmans, A.E., IJsselstijn, H., Rottier, R.J., Wijnen, R., Tibboel, D., and de Klein, A. (2014). Clinical and etiological heterogeneity in patients with tracheo-esophageal malformations and associated anomalies. Eur. J. Med. Genet. *57*, 440–452. https://doi.org/10.1016/j.ejmg.2014.05.009.
8. Li, Y., Litingtung, Y., Ten Dijke, P., and Chiang, C. (2007). Aberrant Bmp signaling and notochord delamination in the pathogenesis of esophageal atresia. Dev. Dyn. *236*, 746–754. https://doi.org/10.1002/dvdy.21075.
9. Goss, A.M., Tian, Y., Tsukiyama, T., Cohen, E.D., Zhou, D., Lu, M.M., Yamaguchi, T.P., and Morrisey, E.E. (2009). Wnt2/2b and beta-catenin signaling are necessary and sufficient to specify lung progenitors in the foregut. Dev. Cell *17*, 290–298. https://doi.org/10.1016/j.devcel.2009.06.005.
10. Harris-Johnson, K.S., Domyan, E.T., Vezina, C.M., and Sun, X. (2009). beta-Catenin promotes respiratory progenitor identity in mouse foregut. Proc. Natl. Acad. Sci. USA *106*, 16287–16292. https://doi.org/10.1073/pnas.0902274106.
11. Rankin, S.A., Han, L., McCracken, K.W., Kenny, A.P., Anglin, C.T., Grigg, E.A., Crawford, C.M., Wells, J.M., Shannon, J.M., and Zorn, A.M. (2016). A Retinoic Acid-Hedgehog Cascade Coordinates Mesoderm-Inducing Signals and Endoderm Competence during Lung Specification. Cell Rep. *16*, 66–78. https://doi.org/10.1016/j.celrep.2016.05.060.
12. Kim, E., Jiang, M., Huang, H., Zhang, Y., Tjota, N., Gao, X., Robert, J., Gilmore, N., Gan, L., and Que, J. (2019). Isl1 Regulation of Nkx2.1 in the Early Foregut Epithelium Is Required for Trachea-Esophageal Separation and Lung Lobation. Dev. Cell *51*, 675–683. https://doi.org/10.1016/j.devcel.2019.11.002.
13. Nasr, T., Mancini, P., Rankin, S.A., Edwards, N.A., Agricola, Z.N., Kenny, A.P., Kinney, J.L., Daniels, K., Vardanyan, J., Han, L., et al. (2019). Endosome-Mediated Epithelial Remodeling Downstream of Hedgehog-Gli Is Required for Tracheoesophageal Separation. Dev. Cell *51*, 665–674. https://doi.org/10.1016/j.devcel.2019.11.003.
14. Cote, L.E., and Feldman, J.L. (2022). Won't You be My Neighbor: How Epithelial Cells Connect Together to Build Global Tissue Polarity. Front. Cell Dev. Biol. *10*, 887107. https://doi.org/10.3389/fcell.2022.887107.
15. Pickett, M.A., Naturale, V.F., and Feldman, J.L. (2019). A Polarizing Issue: Diversity in the Mechanisms Underlying Apico-Basolateral Polarization In Vivo. Annu. Rev. Cell Dev. Biol. *35*, 285–308. https://doi.org/10.1146/annurev-cellbio-100818-125134.
16. Aigouy, B., and Le Bivic, A. (2016). The PCP pathway regulates Baz planar distribution in epithelial cells. Sci. Rep. *6*, 33420. https://doi.org/10.1038/srep33420.
17. Murdoch, J.N., Doudney, K., Paternotte, C., Copp, A.J., and Stanier, P. (2001). Severe neural tube defects in the loop-tail mouse result from mutation of Lpp1, a novel gene involved in floor plate specification. Hum. Mol. Genet. *10*, 2593–2601. https://doi.org/10.1093/hmg/10.22.2593.
18. Butler, M.T., and Wallingford, J.B. (2018). Spatial and temporal analysis of PCP protein dynamics during neural tube closure. eLife *7*, e36456. https://doi.org/10.7554/eLife.36456.
19. Torban, E., Wang, H.J., Patenaude, A.M., Riccomagno, M., Daniels, E., Epstein, D., and Gros, P. (2007). Tissue, cellular and sub-cellular localization of the Vangl2 protein during embryonic development: effect of the Lp mutation. Gene Expr. Patterns *7*, 346–354. https://doi.org/10.1016/j.modgep.2006.07.007.
20. Yarwood, R., Hellicar, J., Woodman, P.G., and Lowe, M. (2020). Membrane trafficking in health and disease. Dis. Model. Mech. *13*, dmm043448. https://doi.org/10.1242/dmm.043448.
21. Zhong, G., Ahimaz, P., Edwards, N.A., Hagen, J.J., Faure, C., Lu, Q., Kingma, P., Middlesworth, W., Khlevner, J., El Fiky, M., et al. (2022). Identification and validation of candidate risk genes in endocytic vesicular trafficking associated with esophageal atresia and tracheoesophageal fistulas. HGG Adv. *3*, 100107. https://doi.org/10.1016/j.xhgg.2022.100107.
22. Szklarczyk, D., Kirsch, R., Koutrouli, M., Nastou, K., Mehryary, F., Hachilif, R., Gable, A.L., Fang, T., Doncheva, N.T., Pyysalo, S., et al. (2023). The STRING database in 2023: protein-protein association networks and functional enrichment analyses for any sequenced genome of interest. Nucleic Acids Res. *51*, D638–D646. https://doi.org/10.1093/nar/gkac1000.
23. Nakayama, T., Fish, M.B., Fisher, M., Oomen-Hajagos, J., Thomsen, G.H., and Grainger, R.M. (2013). Simple and efficient CRISPR/Cas9-mediated targeted mutagenesis in Xenopus tropicalis. Genesis *51*, 835–843. https://doi.org/10.1002/dvg.22720.
24. Guo, X., Zhang, T., Hu, Z., Zhang, Y., Shi, Z., Wang, Q., Cui, Y., Wang, F., Zhao, H., and Chen, Y. (2014). Efficient RNA/Cas9-mediated genome editing in Xenopus tropicalis. Development *141*, 707–714. https://doi.org/10.1242/dev.099853.
25. Miyashita, Y., and Ozawa, M. (2007). Increased Internalization of p120-uncoupled E-cadherin and a Requirement for a Dileucine Motif in the Cytoplasmic Domain for Endocytosis of the Protein. J. Biol. Chem. *282*, 11540–11548. https://doi.org/10.1074/jbc.M608351200.
26. Butler, M.T., and Wallingford, J.B. (2017). Planar cell polarity in development and disease. Nat. Rev. Mol. Cell Biol. *18*, 375–388. https://doi.org/10.1038/nrm.2017.11.
27. Panzica, D.A., Findlay, A.S., van Ladesteijn, R., and Collinson, J.M. (2019). The core planar cell polarity gene, Vangl2, maintains apical-basal organisation of the corneal epithelium. J. Anat. *234*, 106–119. https://doi.org/10.1111/joa.12676.
28. vandenBerg, A.L., and Sassoon, D.A. (2009). Non-canonical Wnt signaling regulates cell polarity in female reproductive tract development via van gogh-like 2. Development *136*, 1559–1570. https://doi.org/10.1242/dev.034066.
29. Devenport, D., Oristian, D., Heller, E., and Fuchs, E. (2011). Mitotic internalization of planar cell polarity proteins preserves tissue polarity. Nat. Cell Biol. *13*, 893–902. https://doi.org/10.1038/ncb2284.

30. Ecker, M., Redpath, G.M.I., Nicovich, P.R., and Rossy, J. (2021). Quantitative visualization of endocytic trafficking through photoactivation of fluorescent proteins. Mol. Biol. Cell *32*, 892–902. https://doi.org/10.1091/mbc.E20-10-0669.

31. Puri, C., Vicinanza, M., Ashkenazi, A., Gratian, M.J., Zhang, Q., Bento, C. F., Renna, M., Menzies, F.M., and Rubinsztein, D.C. (2018). The RAB11A-Positive Compartment Is a Primary Platform for Autophagosome Assembly Mediated by WIPI2 Recognition of PI3P-RAB11A. Dev. Cell *45*, 114–131. https://doi.org/10.1016/j.devcel.2018.03.008.

32. Yang, Q., Li, G., Singh, S.K., Alexander, E.A., and Schwartz, J.H. (2006). Vacuolar H+ -ATPase B1 subunit mutations that cause inherited distal renal tubular acidosis affect proton pump assembly and trafficking in inner medullary collecting duct cells. J. Am. Soc. Nephrol. *17*, 1858–1866. https://doi.org/10.1681/ASN.2005121277.

33. Dong, X., Li, H., Derdowski, A., Ding, L., Burnett, A., Chen, X., Peters, T.R., Dermody, T.S., Woodruff, E., Wang, J.J., et al. (2005). AP-3 directs the intracellular trafficking of HIV-1 Gag and plays a key role in particle assembly. Cell *120*, 663–674. https://doi.org/10.1016/j.cell.2004.12.023.

34. Kantheti, P., Qiao, X., Diaz, M.E., Peden, A.A., Meyer, G.E., Carskadon, S. L., Kapfhamer, D., Sufalko, D., Robinson, M.S., Noebels, J.L., et al. (1998). Mutation in AP-3 delta in the mocha mouse links endosomal transport to storage deficiency in platelets, melanosomes, and synaptic vesicles. Neuron *21*, 111–122. https://doi.org/10.1016/s0896-6273(00)80519-x.

35. Dubois, T., Paléotti, O., Mironov, A.A., Fraisier, V., Stradal, T.E.B., De Matteis, M.A., Franco, M., and Chavrier, P. (2005). Golgi-localized GAP for Cdc42 functions downstream of ARF1 to control Arp2/3 complex and F-actin dynamics. Nat. Cell Biol. *7*, 353–364. https://doi.org/10.1038/ncb1244.

36. Gryaznova, T., Gubar, O., Burdyniuk, M., Kropyvko, S., and Rynditch, A. (2018). WIP/ITSN1 complex is involved in cellular vesicle trafficking and formation of filopodia-like protrusions. Gene *674*, 49–56. https://doi.org/10.1016/j.gene.2018.06.078.

37. Wang, J., Ahimaz, P.R., Hashemifar, S., Khlevner, J., Picoraro, J.A., Middlesworth, W., Elfiky, M.M., Que, J., Shen, Y., and Chung, W.K. (2021). Novel candidate genes in esophageal atresia/tracheoesophageal fistula identified by exome sequencing. Eur. J. Hum. Genet. *29*, 122–130. https://doi.org/10.1038/s41431-020-0680-2.

38. Zhang, R., Gehlen, J., Kawalia, A., Melissari, M.T., Dakal, T.C., Menon, A. M., Höfele, J., Riedhammer, K., Waffenschmidt, L., Fabian, J., et al. (2020). Human exome and mouse embryonic expression data implicate ZFHX3, TRPS1, and CHD7 in human esophageal atresia. PLOS One *15*, e0234246. https://doi.org/10.1371/journal.pone.0234246.

39. Lee, J.Y., and Harland, R.M. (2010). Endocytosis is required for efficient apical constriction during Xenopus gastrulation. Curr. Biol. *20*, 253–258. https://doi.org/10.1016/j.cub.2009.12.021.

40. Ossipova, O., Kim, K., Lake, B.B., Itoh, K., Ioannou, A., and Sokol, S.Y. (2014). Role of Rab11 in planar cell polarity and apical constriction during vertebrate neural tube closure. Nat. Commun. *5*, 3734. https://doi.org/10.1038/ncomms4734.

41. Ossipova, O., Chuykin, I., Chu, C.W., and Sokol, S.Y. (2015). Vangl2 cooperates with Rab11 and Myosin V to regulate apical constriction during vertebrate gastrulation. Development *142*, 99–107. https://doi.org/10.1242/dev.111161.

42. Seifert, A.W., Harfe, B.D., and Cohn, M.J. (2008). Cell lineage analysis demonstrates an endodermal origin of the distal urethra and perineum. Dev. Biol. *318*, 143–152. https://doi.org/10.1016/j.ydbio.2008.03.017.

43. Martin, P., and Swanson, G.J. (1993). Descriptive and Experimental Analysis of the Epithelial Remodellings That Control Semicircular Canal Formation in the Developing Mouse Inner Ear. Dev. Biol. *159*, 549–558. https://doi.org/10.1006/dbio.1993.1263.

44. Alsina, B., and Whitfield, T.T. (2017). Sculpting the labyrinth: Morphogenesis of the developing inner ear. Semin. Cell Dev. Biol. *65*, 47–59. https://doi.org/10.1016/j.semcdb.2016.09.015.

45. Flasse, L., Yennek, S., Cortijo, C., Barandiaran, I.S., Kraus, M.R.C., and Grapin-Botton, A. (2020). Apical Restriction of the Planar Cell Polarity Component VANGL in Pancreatic Ducts Is Required to Maintain Epithelial Integrity. Cell Rep. *31*, 107677. https://doi.org/10.1016/j.celrep.2020.107677.

46. Paramore, S.V., Trenado-Yuste, C., Sharan, R., Nelson, C.M., and Devenport, D. (2024). Vangl-dependent mesenchymal thinning shapes the distal lung during murine sacculation. Dev. Cell *59*, 1302–1316. https://doi.org/10.1016/j.devcel.2024.03.010.

47. Paramore, S.V., Goodwin, K., Fowler, E.W., Devenport, D., and Nelson, C. M. (2024). Mesenchymal Vangl1 and Vangl2 facilitate airway elongation and widening independently of the planar cell polarity complex. Development *151*, dev202692. https://doi.org/10.1242/dev.202692.

48. Barlow, H.R., Ahuja, N., Bierschenk, T., Htike, Y., Fassetta, L., Azizoglu, D. B., Flores, J., Gao, N., De la O, S., Sneddon, J.B., et al. (2023). Rab11 is essential to pancreas morphogenesis, lumen formation and endocrine mass. Dev. Biol. *499*, 59–74. https://doi.org/10.1016/j.ydbio.2023.05.002.

49. Niethamer, T.K., and Bush, J.O. (2019). Getting direction(s): The Eph/ephrin signaling system in cell positioning. Dev. Biol. *447*, 42–57. https://doi.org/10.1016/j.ydbio.2018.01.012.

50. Lewis, A.E., Kuwahara, A., Franzosi, J., and Bush, J.O. (2022). Tracheal separation is driven by NKX2-1-mediated repression of Efnb2 and regulation of endodermal cell sorting. Cell Rep. *38*, 110510. https://doi.org/10.1016/j.celrep.2022.110510.

51. Lewis, A.E., Hwa, J., Wang, R., Soriano, P., and Bush, J.O. (2015). Neural crest defects in ephrin-B2 mutant mice are non-autonomous and originate from defects in the vasculature. Dev. Biol. *406*, 186–195. https://doi.org/10.1016/j.ydbio.2015.08.021.

52. Yu, S., Yehia, G., Wang, J., Stypulkowski, E., Sakamori, R., Jiang, P., Hernandez-Enriquez, B., Tran, T.S., Bonder, E.M., Guo, W., et al. (2014). Global ablation of the mouse Rab11a gene impairs early embryogenesis and matrix metalloproteinase secretion. J. Biol. Chem. *289*, 32030–32043. https://doi.org/10.1074/jbc.M113.538223.

53. Ferguson, S.M., Raimondi, A., Paradise, S., Shen, H., Mesaki, K., Ferguson, A., Destaing, O., Ko, G., Takasaki, J., Cremona, O., et al. (2009). Coordinated actions of actin and BAR proteins upstream of dynamin at endocytic clathrin-coated pits. Dev. Cell *17*, 811–822. https://doi.org/10.1016/j.devcel.2009.11.005.

54. Iliescu, A., Gravel, M., Horth, C., and Gros, P. (2014). Independent mutations at Arg181 and Arg274 of Vangl proteins that are associated with neural tube defects in humans decrease protein stability and impair membrane targeting. Biochemistry *53*, 5356–5364. https://doi.org/10.1021/bi500400g.

55. Merello, E., Mascelli, S., Raso, A., Piatelli, G., Consales, A., Cama, A., Kibar, Z., Capra, V., and Marco, P.D. (2015). Expanding the mutational spectrum associated to neural tube defects: literature revision and description of novel VANGL1 mutations. Birth Defects Res. A Clin. Mol. Teratol. *103*, 51–61. https://doi.org/10.1002/bdra.23305.

56. Papakrivopoulou, E., Vasilopoulou, E., Lindenmeyer, M.T., Pacheco, S., Brzóska, H.Ł., Price, K.L., Kolatsi-Joannou, M., White, K.E., Henderson, D.J., Dean, C.H., et al. (2018). Vangl2, a planar cell polarity molecule, is implicated in irreversible and reversible kidney glomerular injury. J. Pathol. *246*, 485–496. https://doi.org/10.1002/path.5158.

57. Schnell, U., and Carroll, T.J. (2016). Planar cell polarity of the kidney. Exp. Cell Res. *343*, 258–266. https://doi.org/10.1016/j.yexcr.2014.11.003.

58. Yuan, Y., Gao, Y., Wang, H., Ma, X., Ma, D., and Huang, G. (2014). Promoter methylation and expression of the VANGL2 gene in the myocardium of pediatric patients with tetralogy of fallot. Birth Defects Res. A Clin. Mol. Teratol. *100*, 973–984. https://doi.org/10.1002/bdra.23291.

59. Li, D., and Wang, J. (2018). Planar Cell Polarity Signaling in Mammalian Cardiac Morphogenesis. Pediatr. Cardiol. *39*, 1052–1062. https://doi.org/10.1007/s00246-018-1860-5.

60. Yates, L.L., and Dean, C.H. (2011). Planar polarity: A new player in both lung development and disease. Organogenesis *7*, 209–216. https://doi.org/10.4161/org.7.3.18462.

61. Wlizla, M., McNamara, S., and Horb, M.E. (2018). Generation and Care of Xenopus laevis and Xenopus tropicalis Embryos. Methods Mol. Biol. *1865*, 19–32. https://doi.org/10.1007/978-1-4939-8784-9_2.

62. Moreno-Mateos, M.A., Vejnar, C.E., Beaudoin, J.D., Fernandez, J.P., Mis, E.K., Khokha, M.K., and Giraldez, A.J. (2015). CRISPRscan: designing highly efficient sgRNAs for CRISPR-Cas9 targeting in vivo. Nat. Methods *12*, 982–988. https://doi.org/10.1038/nmeth.3543.

63. Shen, M.W., Arbab, M., Hsu, J.Y., Worstell, D., Culbertson, S.J., Krabbe, O., Cassa, C.A., Liu, D.R., Gifford, D.K., and Sherwood, R.I. (2018). Predictable and precise template-free CRISPR editing of pathogenic variants. Nature *563*, 646–651. https://doi.org/10.1038/s41586-018-0686-x.

64. Naert, T., Tulkens, D., Edwards, N.A., Carron, M., Shaidani, N.I., Wlizla, M., Boel, A., Demuynck, S., Horb, M.E., Coucke, P., et al. (2020). Maximizing CRISPR/Cas9 phenotype penetrance applying predictive modeling of editing outcomes in Xenopus and zebrafish embryos. Sci. Rep. *10*, 14662. https://doi.org/10.1038/s41598-020-71412-0.

65. Concordet, J.-P., and Haeussler, M. (2018). CRISPOR: intuitive guide selection for CRISPR/Cas9 genome editing experiments and screens. Nucleic Acids Res. *46*, W242–W245. https://doi.org/10.1093/nar/gky354.

66. DeLay, B.D., Corkins, M.E., Hanania, H.L., Salanga, M., Deng, J.M., Sudou, N., Taira, M., Horb, M.E., and Miller, R.K. (2018). Tissue-Specific Gene Inactivation in Xenopus laevis: Knockout of lhx1 in the Kidney with CRISPR/Cas9. Genetics *208*, 673–686. https://doi.org/10.1534/genetics.117.300468.

67. Brinkman, E.K., Chen, T., Amendola, M., and van Steensel, B. (2014). Easy quantitative assessment of genome editing by sequence trace decomposition. Nucleic Acids Res. *42*, e168. https://doi.org/10.1093/nar/gku936.

68. Higashi, T., Arnold, T.R., Stephenson, R.E., Dinshaw, K.M., and Miller, A.L. (2016). Maintenance of the Epithelial Barrier and Remodeling of Cell-Cell Junctions during Cytokinesis. Curr. Biol. *26*, 1829–1842. https://doi.org/10.1016/j.cub.2016.05.036.

69. Sterner, Z.R., Rankin, S.A., Wlizla, M., Choi, J.A., Luedeke, D.M., Zorn, A.M., and Buchholz, D.R. (2019). Novel vectors for functional interrogation of Xenopus ORFeome coding sequences. Genesis *57*, e23329. https://doi.org/10.1002/dvg.23329.

70. Franco, M., and Carmena, A. (2019). Measurement of Mitotic Spindle Angle and Mitotic Cell Distance in Fixed Tissue of Drosophila Larval Brains. Bio Protoc. *9*, e3432. https://doi.org/10.21769/BioProtoc.3432.

STAR★METHODS

KEY RESOURCES TABLE

REAGENT or RESOURCE	SOURCE	IDENTIFIER
Antibodies		
Rabbit anti-PKC zeta	Abcam	Cat#ab59364; RRID: AB_944858
Mouse anti-Cdh1	Developmental Studies Hybridoma Bank	Clone 5D3 (deposited to the DSHB by Gumbiner, B.M.);RRID: AB_528116
Rabbit anti-Dnm2	Abcam	Cat#ab65556; RRID: AB_1603781
Rabbit anti-Rab5a	Cell Signaling Technology	Cat#3547; RRID: AB_2300649
Rabbit anti-Rab11a	Thermo Fisher Scientific	Cat#700184; RRID: AB_2532295
Mouse anti-Rab11a	BD Biosciences	Cat#610657; RRID: AB_397984
Rabbit anti-Tjp1 (ZO-1)	Thermo Fisher Scientific	Cat#61-7300; RRID: AB_138452
Rabbit anti-Par3	Millipore	Cat#07-330; RRID: AB_2101325
Mouse anti-Tuba4b	Sigma	Cat#T9026; RRID: AB_477593
Rabbit anti-Lama1	Sigma	Cat#L9393; RRID: AB_477163
Rabbit anti-pHH3 (Ser10)	Cell Signaling Technology	Cat#9701; RRID: AB_331535
Rabbit anti-Vangl2	Sergei Sokol[41]	RRID: AB_2744499
Rabbit anti-Celsr1	BiCell Scientific	Cat#50801
Mouse anti-Sox2	Abcam	Cat#ab79351; RRID: AB_10710406
Rabbit anti-Nkx2-1	Santa Cruz	Cat# c-13040; RRID: AB_793532
Goat anti-Foxf1	R&D Systems	Cat#AF4798; RRID: AB_2105588
Rabbit anti-Itsn1	Millipore	Cat#ABS984
Donkey anti-mouse AF488	Thermo Fisher Scientific	Cat#A-21202; RRID: AB_141607
Donkey anti-goat AF568	Thermo Fisher Scientific	Cat#A-11057; RRID: AB_2534104
Donkey anti-rabbit AF647	Thermo Fisher Scientific	Cat#A-31573; RRID: AB_2536183
Donkey anti-rabbit AF568	Thermo Fisher Scientific	Cat#A10042; RRID: AB_2534017
Donkey anti-mouse AF647	Thermo Fisher Scientific	Cat#A-31571; RRID: AB_162542
Chemicals, peptides, and recombinant proteins		
Cas9 protein	PNA Biosciences	Cat#CP01-50
Doxycycline hyclate	Sigma	Cat#D9891
GeneArt mutagenesis kit	Thermo Fisher Scientific	Cat#A13282
Accuprime Taq	Thermo Fisher Scientific	Cat#12339016
Phusion High Fidelity PCR Master Mix	Thermo Fisher Scientific	Cat#F531L
pCR8-Gateway TOPO vector	Thermo Fisher Scientific	Cat#K250020
Gateway LR Clonase II Plus	Thermo Fisher Scientific	Cat#12538120
I-SceI	New England Biolabs	Cat#R0694S
Normal donkey serum	Jackson Immuno Research Laboratories	Cat#017-000-121
Experimental models: Organisms/strains		
Xenopus laevis: wild type females	NASCO	Cat#LM00531
Xenopus laevis: wild type males	NASCO	Cat#LM00715
Xenopus tropicalis: wild type females	Xenopus1	N/A
Xenopus tropicalis: wild type males	Xenopus1	N/A
Xenopus laevis: Xla.Tg(CMV:memGFP; cryga:mCherry)^{NXR}	National Xenopus Resource	NXR_0012
Xenopus tropicalis: Xtr.sox2^{tmHorb}	National Xenopus Resource	NXR_3051
Oligonucleotides		
rab11a.S gRNA: GAGATTACTCTTCCCCACAC	Nasr et al.[13]	N/A

(*Continued on next page*)

Continued

REAGENT or RESOURCE	SOURCE	IDENTIFIER
slc45a2 gRNA: GGTTACATAGGCTGCCTCCA	Delay et al.[66]	N/A
gRNA for CRISPR experiments: see Table S3	This paper	N/A
Primers for CRISPR genotyping: see Table S3	This paper	N/A
Recombinant DNA		
pCS2+ Xenopus Cdh1-3xGFP	Higashi et al.[68]	N/A
pCS2+ Xenopus Cdh1-ΔLL-3xGFP	This study	N/A
pDXTR	Sterner et al.[69]	N/A
pDXTP-*hhex*;rtTA	Nasr et al.[13]	N/A
Software and algorithms		
NIS Elements	Nikon	RRID: SCR_014329
ImageJ	National Institutes of Health	RRID: SCR_003070
IMARIS	Oxford Instruments	RRID: SCR_007370
Surface-Surface Contact Area XTension	Oxford Instruments	https://imaris.oxinst.com/open/view/surface-surface-contact-area
Inference of CRISPR edits (ICE)	Synthego	https://ice.editco.bio
Tracking of Indels by Decomposition (TIDE)	Brinkman et al.[67]	https://tide.nki.nl
InDelphi	Shen et al.[63]	https://indelphi.giffordlab.mit.edu
CRISPRScan	Moreno-Mateos et al.[62]	https://www.crisprscan.org
CRISPOR	Concordet and Haeussler[65]	https://crispor.gi.ucsc.edu
ImageLab	BioRad	RRID: SCR_014210
Prism 10	GraphPad	RRID: SCR_002798

EXPERIMENTAL MODEL AND STUDY PARTICIPANT DETAILS

Xenopus husbandry and experiments were performed using Cincinnati Children's Hospital Medical Center (CCHMC) Institutional Animal Care and Use Committee (IACUC 2022-0026) approved guidelines. Wild type adult female and male *Xenopus tropicalis* and *Xenopus laevis* frogs were purchased from NASCO and Xenopus1 (USA) and housed in the CCHMC vivarium under standard housing conditions with a 12-hour light-dark cycle in a recirculating aquatic system. *Xenopus* embryos were obtained by *in vitro* fertilization according to standard procedures.[61] Transgenic membrane GFP female *Xenopus laevis* (*Xla.Tg(CMV:memGFP;cryga:mCherry)*^{NXR}) were purchased from the National Xenopus Resource (RRID: NXR_0012). *Sox2* germline mutant embryos were generated at the National *Xenopus* Resource according to standard procedures (RRID: SCR_013731). Healthy adult frogs were used for experiments, and embryos were randomly assigned to experimental groups for gene editing experiments.

CRISPR-Cas9 gene editing and Xenopus embryo culture

Guide RNAs and genotyping primers were designed using CRISPRScan,[62] InDelphi,[63] and CRISPOR predictive algorithms[64,65] and synthesized as altR-crRNA by IDT (sequences in key resources table and Table S3). Guide RNA sequences that maximized predictive efficiency (CRISPRScan) and high percentage of predicted out of frame indel mutations (InDelphi) were selected. After annealing with tracrRNA to create a single gRNA, gRNAs were combined with recombinant Cas9 protein (PNA Biosciences) and injected into 1-2 cell stage *Xenopus* embryos at a final concentration of 500-700pg gRNA and 1-1.5ng Cas9p. *Xenopus tropicalis* embryos were raised at 25°C in 0.1X Modified Barth's solution (MBS) for three days post fertilization before being anesthetized and fixed at NF44 in MEMFA (3.7% formaldehyde, 0.1M MOPS, 2mM EGTA, 1mM $MgSO_4$) for 1hr at room temperature, then in Dent's solution (80% methanol, 20% DMSO) for long term storage at -20°C. *Xenopus laevis* embryos were raised between 15-21°C in 0.1X MBS for 3-5 days post fertilization (to stages NF37-44), then anesthetized and fixed in MEMFA or 2% trichloroacetic acid (for endosome proteins and Vangl2 immunostaining) for 30-40 mins at room temperature. Embryos were immunostained and imaged by confocal microscopy as outlined below prior to genotyping.

Genotype-phenotype scoring

Genotyping for CRISPR-Cas9 editing efficiency in individual CRISPR-edited embryos was performed as described in Zhong et al. [21] using the primer sequences in Table S3 (*slc45a2* sequence from Delay et al.[66]). PCR amplified products from individual embryos were sent for Sanger sequencing at the DNA Sequencing Facility at CCHMC. Sanger sequences were deconvoluted using Inference of

CRISPR Edits (Synthego, USA) or Tracking of Indels by Decomposition (Brinkman et al.[67]) to determine percent indel efficiency (percent of mutations in each embryo) and mosaicism (different types of indel mutations in a given embryo) (Figure S1). Only embryos with >40% indel efficiency were considered in genotype-phenotype analysis, as if the mutation burden was less than this, we concluded that the gene was not sufficiently mutated to test its function. A minimum of 20 individual mutant embryos from 3 independent editing experiments were analyzed to identify a statistically significant frequency of trachea-esophageal anomalies by Student's t-test from the 2% baseline detected in controls. Individual genotype-phenotype scoring and mutation efficiencies are provided in Table S2.

E-Cadherin (Cdh1) site-directed mutagenesis and *Xenopus* transgenesis

pCS2+ *Xenopus* E-cadherin-3xGFP was a gift from Ann Miller (University of Michigan) and described in Higashi et al.[68] A dileucine motif (LL) in the evolutionarily conserved juxta-membrane cytoplasmic domain of E-cadherin is required for E-cadherin endocytosis.[25] Site-directed mutagenesis was performed with the GeneArt Mutagenesis kit (ThermoFisher A13282 with Accuprime Taq Polymerase, ThermoFisher 12339016) using the following primers (mutant sequence bold, underlined; wt sequence TTA CTA encodes LL, mutation GCA GCG encodes AA to mutate these two leucines (LL) at positions 732, 733 into alanines (AA) of *Xenopus* E-cadherin.

Forward mutagenic primer:
5'- GTG GTA AAA GAG CCT **GCA** **GCG** CCT CCA GAA GGC GAC -3'
Reverse mutagenic primer:
3'- CAC CAT TTT CTC GGA **CGT** **CGC** GGA GGT CTT CCG CTG -5'
Mutagenesis was confirmed with the following sequencing primers:
Forward sequencing primer: 5' GAG CTG GAG ATT GGT CAA TAC G 3';
Reverse sequencing primer: 5′ GAG CCA CTG CCT TCA TAA TCG 3′.

Following confirmation of mutagenesis, both the Cdh1-GFP wild type and mutant (LL>AA) were cloned into the pCR8-Gateway TOPO vector (ThermoFisher K250020) according to manufacturer's instructions. Gateway LR Clonase II Plus (ThermoFisher 12538120) was then used in standard recombination reactions according to manufacturer's instructions to transfer the *EcadGFP wild type and mutant (LL>AA)* into the pDXTR transgenesis responder plasmid,[69] which enables DOX-dependent expression.

Transgenic embryos were generated as follows: 250pg of pDXTP-*hhex* promoter:rtTA (Nasr et al.,[13]) and 500pg of pDXTR-EcadGFP (wt or LL>AA mutant) were incubated in a 25uL reaction containing 2.5μL of I-SceI meganuclease enzyme (New England Biolabs #R0694S) in 0.5X I-SceI buffer. The reaction was incubated at 37°C for 40 minutes and then 5nL of this reaction mix was immediately injected into 1-cell embryos on either side of the sperm entry point within the first 60–75 minutes after fertilization. Embryos were cultured at 13–15°C for the first two to three hours after injection and subsequently at 18°C to 23°C degrees thereafter. Transgenic embryos were selected based on GFP fluorescence in the eye, which becomes visible during early tailbud stages.[69] Transgenes were activated by the addition of doxycycline (Sigma #D9891) at a final concentration of 50μg/mL to the embryo culture buffer (0.1X MBS). Culturing of un-injected embryos in this dose of DOX has no noticeable effect on embryonic development or tracheal-esophageal separation. Transgenic efficiency (embryos with GFP+ eyes at tailbud stages NF33-35) ranged from approximately 8% to 16%, consistent with previous transgenic studies.[13,69]

METHOD DETAILS

Whole mount immunostaining and confocal microscopy

Whole mount immunostaining on *Xenopus* tissue was performed as described in Nasr et al.[13] and Zhong et al.[21] with the following modifications for imaging endosome and polarity proteins: fixed embryos were rehydrated in PBS, embedded in 2% low melt agarose in PBS, and sectioned with a Vibratome VT1000S (Leica) to obtain 200 μm tissue slices containing the trachea and esophagus. Slices were permeabilized with 0.1% Triton X-100 in PBS (0.3% Triton X-100 for anti-Vangl2), blocked in 5% normal donkey serum in PBS, then incubated in primary antibody (1:100) in blocking solution overnight at 4°C. Slices were incubated in Alexa Fluor-conjugated secondary antibody (1:500) in blocking solution for 2 hours at room temperature, then dehydrated in 100% methanol. For confocal microscopy, slices were cleared in BABB and imaged on a Nikon A1 inverted laser scanning confocal microscope with a 10X, 20X water immersion, or 40X oil immersion objective (Nikon USA). For super resolution microscopy, slices were cleared in BABB and imaged on a Nikon AXR confocal microscope with spatial array detector (NSPARC, Nikon, USA) in super resolution mode with 40X and 100X oil immersion objectives.

Image analyses

Signal intensity quantification

Signal intensity quantification was performed in ImageJ (NIH).

Regions of interest (ROI) were drawn around the apical and basal membranes, then mean gray value was measured and plotted as mean intensity ± max/min normalized to the fluorescence intensity of memGFP signal. At least five cells were measured per embryo in a minimum of five embryos per condition for quantification and statistical analysis by 2W-ANOVA.

Prolate ellipticity, surface contact area, and 3D quantification of Cdh1

Prolate ellipticity and surface contact area measurements were performed in Imaris (Bitplane). 3D cell volumes were rendered based on E-Cadherin staining and surface models were generated. Prolate ellipticity was measured from rendered surfaces of epithelial

cells and plotted as mean ± max/min. Values approaching 1 have elongated shapes while values approaching 0 have spherical shapes. Surface-surface contact area between the esophagus and trachea-esophageal septum, within the trachea-esophageal septum, and between the trachea and trachea-esophageal septum was measured from rendered surfaces of epithelial cells using the Surface-Surface Contact Area XTension and plotted as the mean ± max/min. Mean Cdh1 intensity was measured on the rendered surface and normalized to mean memGFP intensity. At least five cells were measured per embryo in a minimum of five embryos per condition for quantification and statistical analysis by unpaired Student's t-test (prolate ellipticity) and 1W-ANOVA (surface contact area).

Three-dimensional measurements of axes in the foregut

Three dimensional lengths of x (medial), y (dorsal-ventral), and z (rostral-caudal) axes were performed in Imaris (Bitplane). 3D cell volumes were rendered based on E-Cadherin staining and surface models were generated. Lengths were measured from rendered surfaces of epithelial cells and plotted as the mean length of each axis ± standard error of the mean. At least five embryos were measured for quantification and statistical analysis by unpaired Student's t-test.

Mitotic spindle orientation

Mitotic spindle orientation angles were obtained in ImageJ (NIH) as described in Franco and Carmena, 2019.[70] Only images with z-sections through the axial axis of *Xenopus* embryos containing clearly identifiable mitotic spindles stained with anti-α-tubulin were analyzed for spindle angles. One line of the angle was drawn through linking both centrosomes, and the second line of the angle was drawn parallel to the basement membrane of the epithelial cell. Measurements were collected and wind rose plots were generated in Excel. At least three mitotic spindles were measured in a minimum of 5 embryos for quantification and statistical analysis was performed by Kolmogorov-Smirnov tests.

Colocalization and nearest neighbor analysis (super resolution)

Pearson colocalization coefficients between Vangl2/Rab11a, Cdh1/Rab11a, and Celsr1/Rab11a immunostaining signals were calculated in Nikon Elements (Nikon USA). ROIs were drawn around an entire cell, and the Pearson colocalization coefficient was determined. A coefficient of 1 indicates two channels whose fluorescence intensities are perfectly linearly related. For super resolution imaging quantification, Rab11a and Vangl2 spots were detected and rendered in Imaris (Bitplane USA). Distances between Rab11a-Vangl2 spots were measured and graphed as a histogram. Vangl2 spots within 500nm of Rab11a spots were considered to be within the Rab11a+ recycling endosome compartment.[30,31]. At least six cells were measured in a minimum of 5 embryos for quantification and statistical analyses by 1W-ANOVA.

Immunoblotting

Whole Xenopus embryos or microdissected anterior foregut tissue (from pharynx to stomach) were pooled and lysed in Triton X-100 lysis buffer (0.5% Triton X-100, 0.1M HEPES, 150 mM NaCl, 2mM EDTA pH 8.0, 2mM EGTA) containing protease inhibitors (ThermoFisher). Protein lysates were combined with 2X Laemmli buffer and 0.1M DTT, boiled, and separated by 4-12% Bis-Tris gel electrophoresis (ThermoFisher). For HRP detection, membranes were blocked in 5% BSA, then incubated in primary antibody (1:1000) overnight in blocking solution at 4°C. Membranes were incubated in HRP-conjugated secondary antibody (1:5000) in blocking solution for 1 hour at room temperature, then visualized by addition of ECL substrate (Amersham, GE) and imaged using a ChemiDoc (BioRad). Western blot quantification was performed in ImageLab (BioRad).

QUANTIFICATION AND STATISTICAL ANALYSIS

Statistical analyses were performed in Prism 10 (GraphPad). Statistical details of experiments can be found in the figure legends including statistical tests used, exact value of experimental replicates, how experimental replicates are defined, and dispersion and precision measures. All experiments were independently replicated a minimum of three times.